Peculiar galaxies

ATLAS OF PECULIAR GALAXIES

HALTON ARP
Mount Wilson and Palomar Observatories
Carnegie Institution of Washington, California Institute of Technology
Received December 27, 1965; revised April 4, 1966

ABSTRACT

The *Atlas of Peculiar Galaxies* presents the results of more than four years of direct photography with the 200-inch telescope. Unusual galaxies were selected from lists by Zwicky, Vorontsov-Velyaminov, and unpublished lists by A. G. Wilson, E. Herzog, Wirtanen, the author, and others. Plate files of Mount Wilson and Palomar Observatories were searched for suitable objects, and some of these plates are reproduced. For the most part, however, limiting, good-seeing exposures were obtained on blue-visual sensitive plates at the prime focus (11".1/mm) of the 200-inch.

The objects are arranged 6 on a page, 57 pages, for a total of 338 objects. Magnifications range from 1× to 10×. They are ordered empirically according to their form and visual appearance, Tabular material presents known data for the objects including positions, plate data, radial velocities when known, references, and remarks on both over-all and detailed peculiarities.

The *Atlas* is also available in large size, 11 × 14-inch photographic reproduction, from the California Institute of Technology Bookstore for a price of about $60 bound.

PREFACE

Forty years after the discovery that galaxies were independent stellar systems, we still have not penetrated very far into the mystery of how they maintain themselves or what physical forces are responsible for shaping their observed forms. The galaxies are the constituent units of mass and energy in the Universe, and yet we are still challenged by such questions as: What causes the characteristic shape of spiral galaxies? How are elliptical galaxies related to spirals? How are galaxies formed, and how do they evolve?

It is difficult to resist an oversimplified impression of what a galaxy is because the Hubble classification divides the galaxies into the well-known categories of smooth, amorphous ellipticals, and flattened spirals with star-studded arms. But far from all galaxies fit the Hubble sequence of nebular forms. In fact, when looked at closely enough, every galaxy is peculiar. Appreciation of these peculiarities is important in order to build a realistic picture of what galaxies are really like. But the peculiarities are also important for the reason that, if we could analyze a galaxy in the laboratory, we would deform it, shock it, probe it in order to discover its properties. The peculiarities of the galaxies pictured in this *Atlas* represent perturbations, deformations, and interactions which should enable us to analyze the nature of the real galaxies which we observe and which are too remote to experiment on directly. In general, the more conspicuous the peculiarity, the more illustrative it is of special events and reactions that occur in galaxies. From this range of experiments which nature furnishes us, then, it is our task to select and study which will give the most insight into the composition and structure and the forces which govern a galaxy.

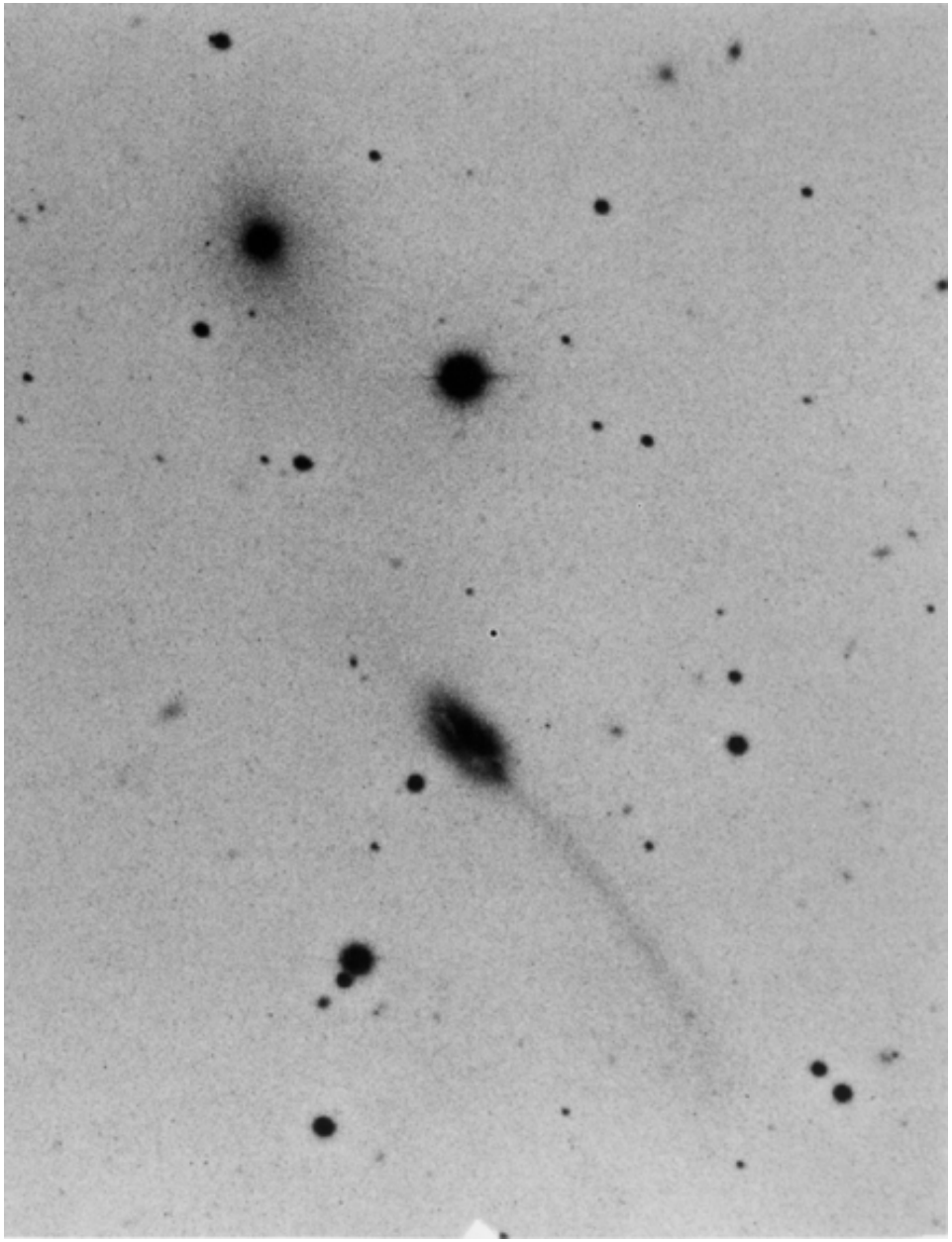

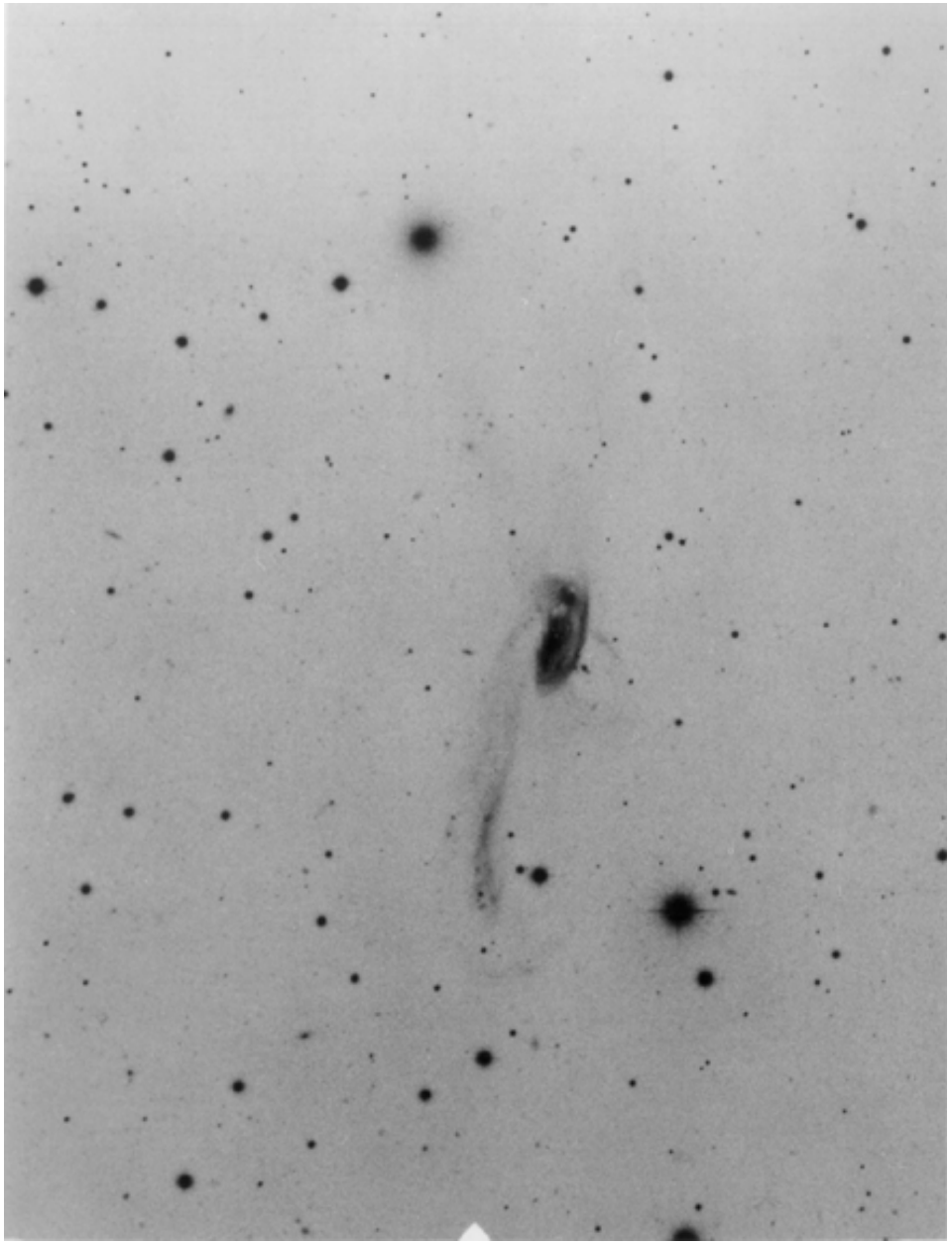

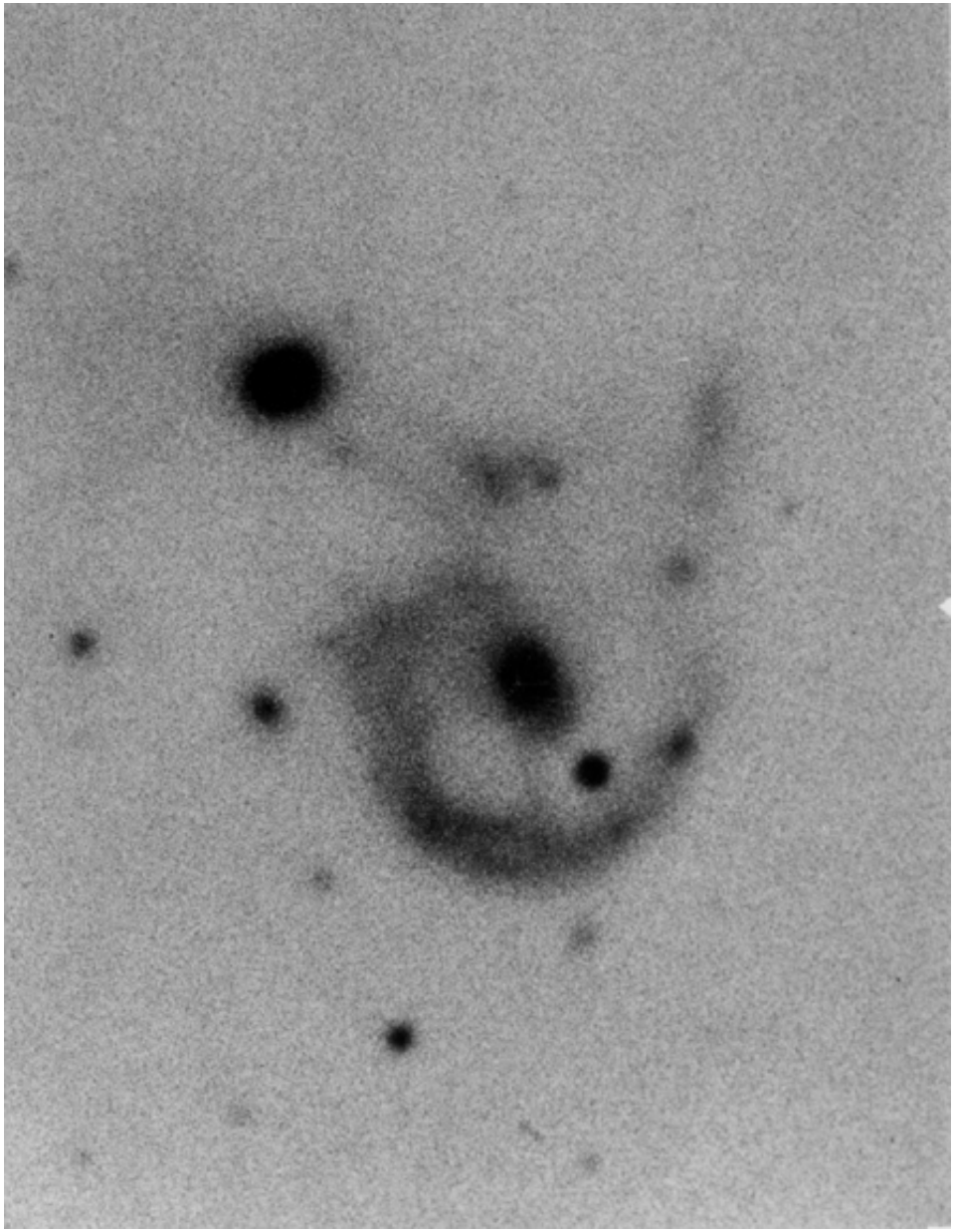

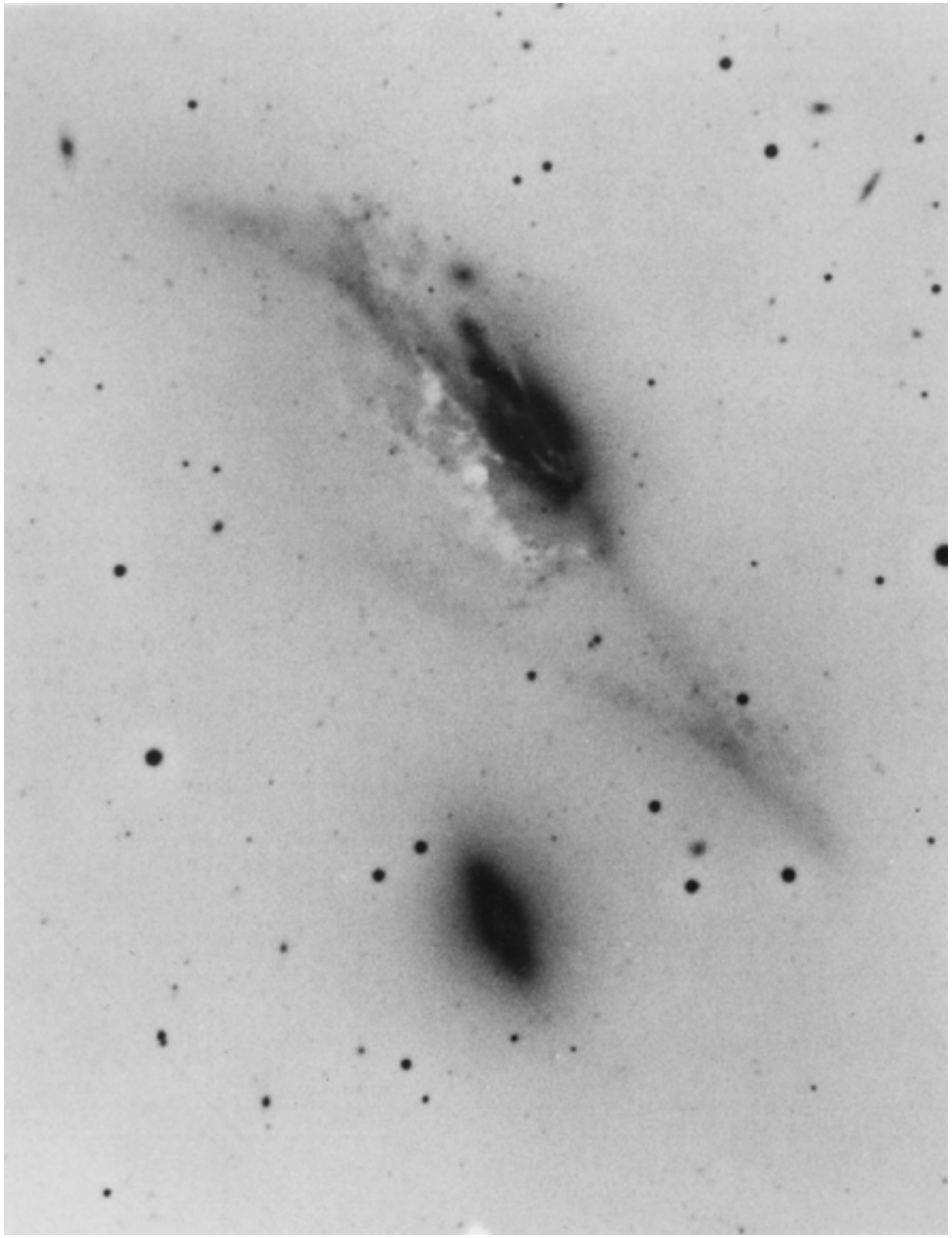

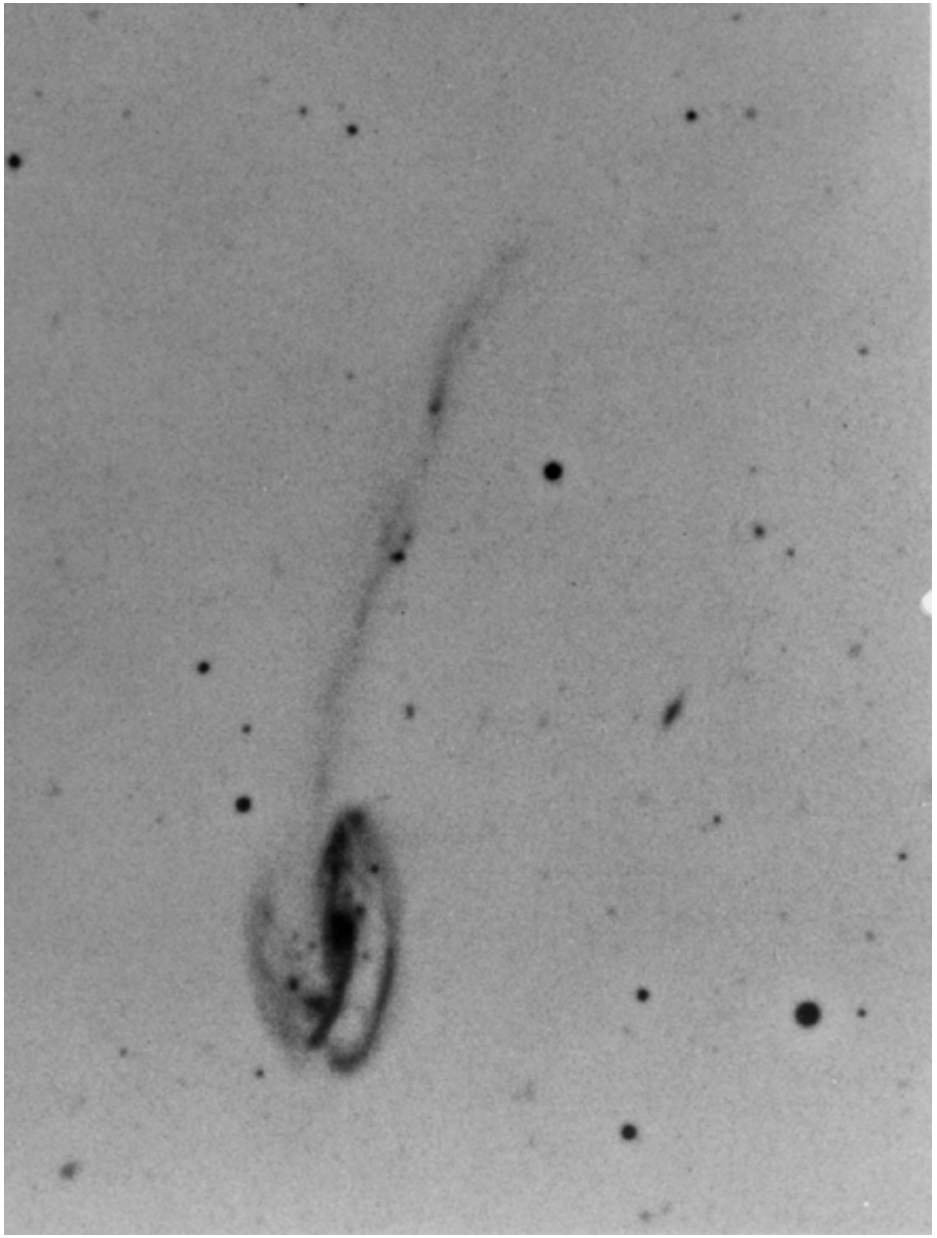

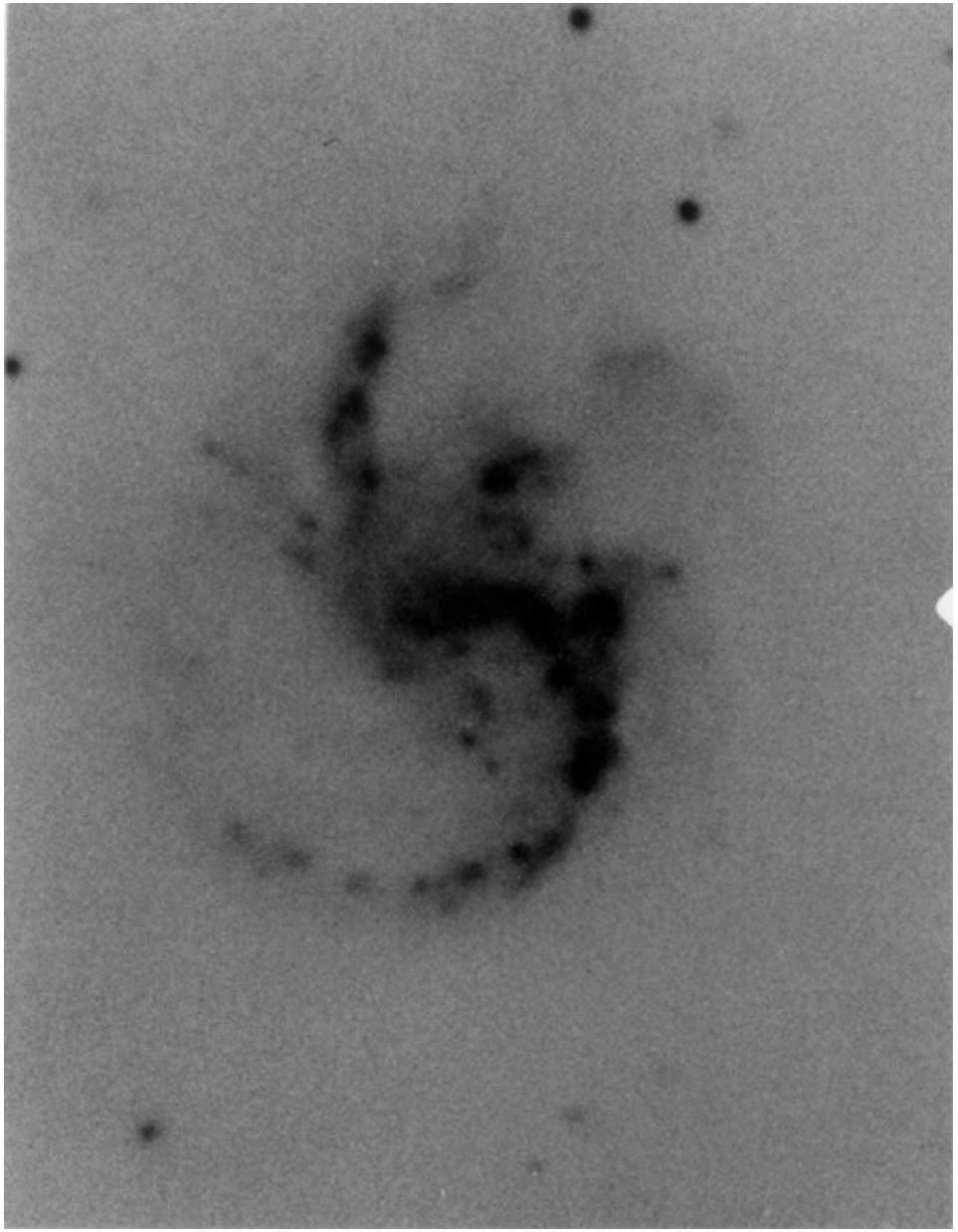

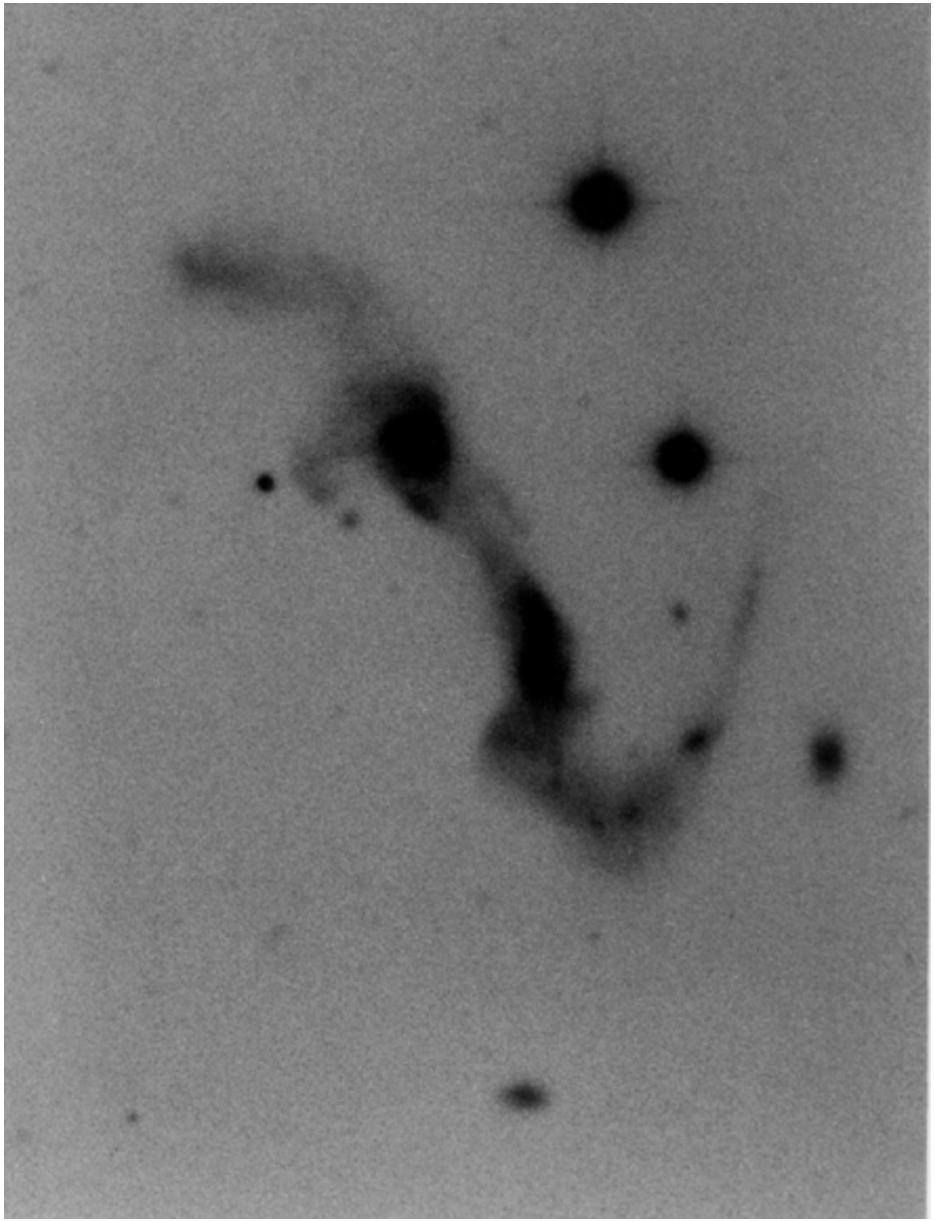

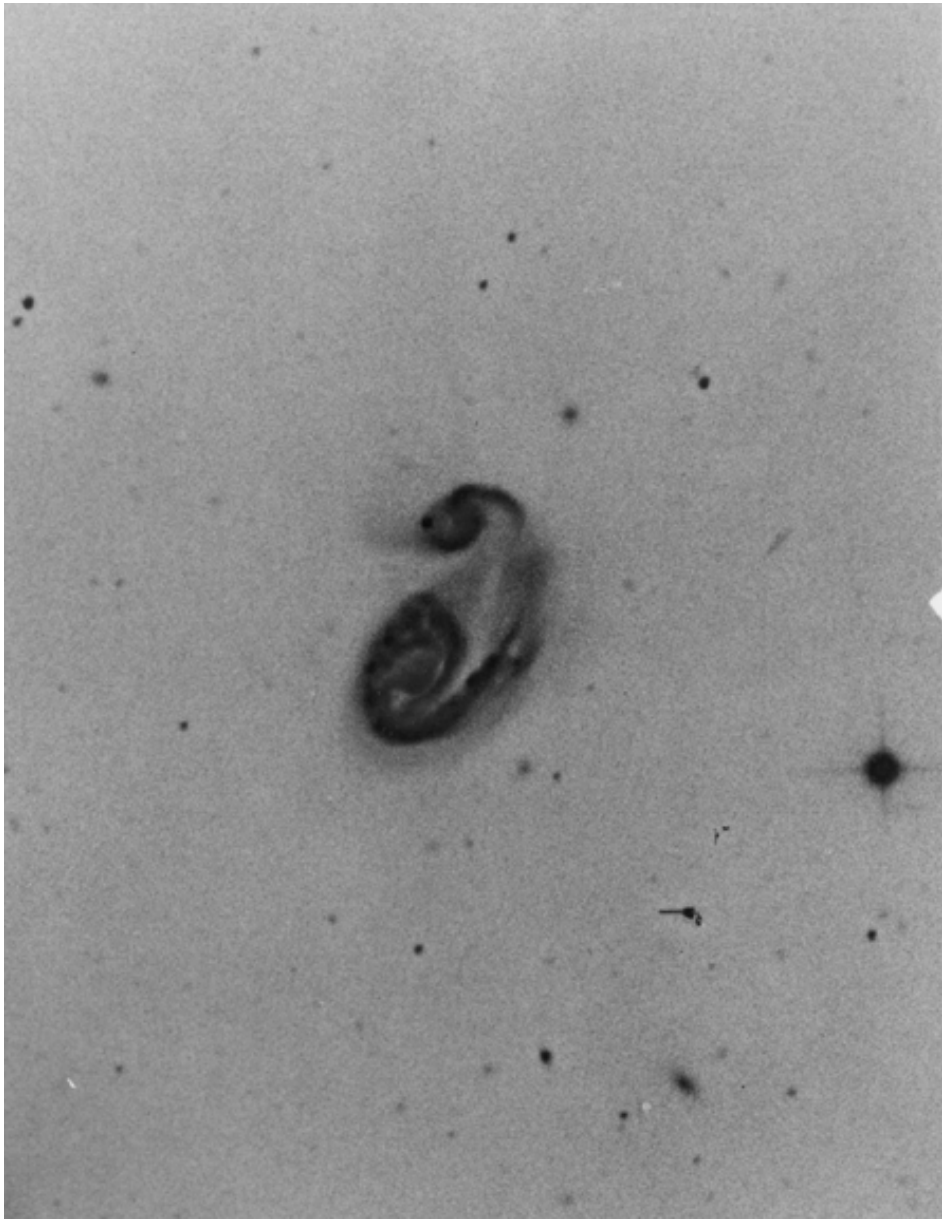

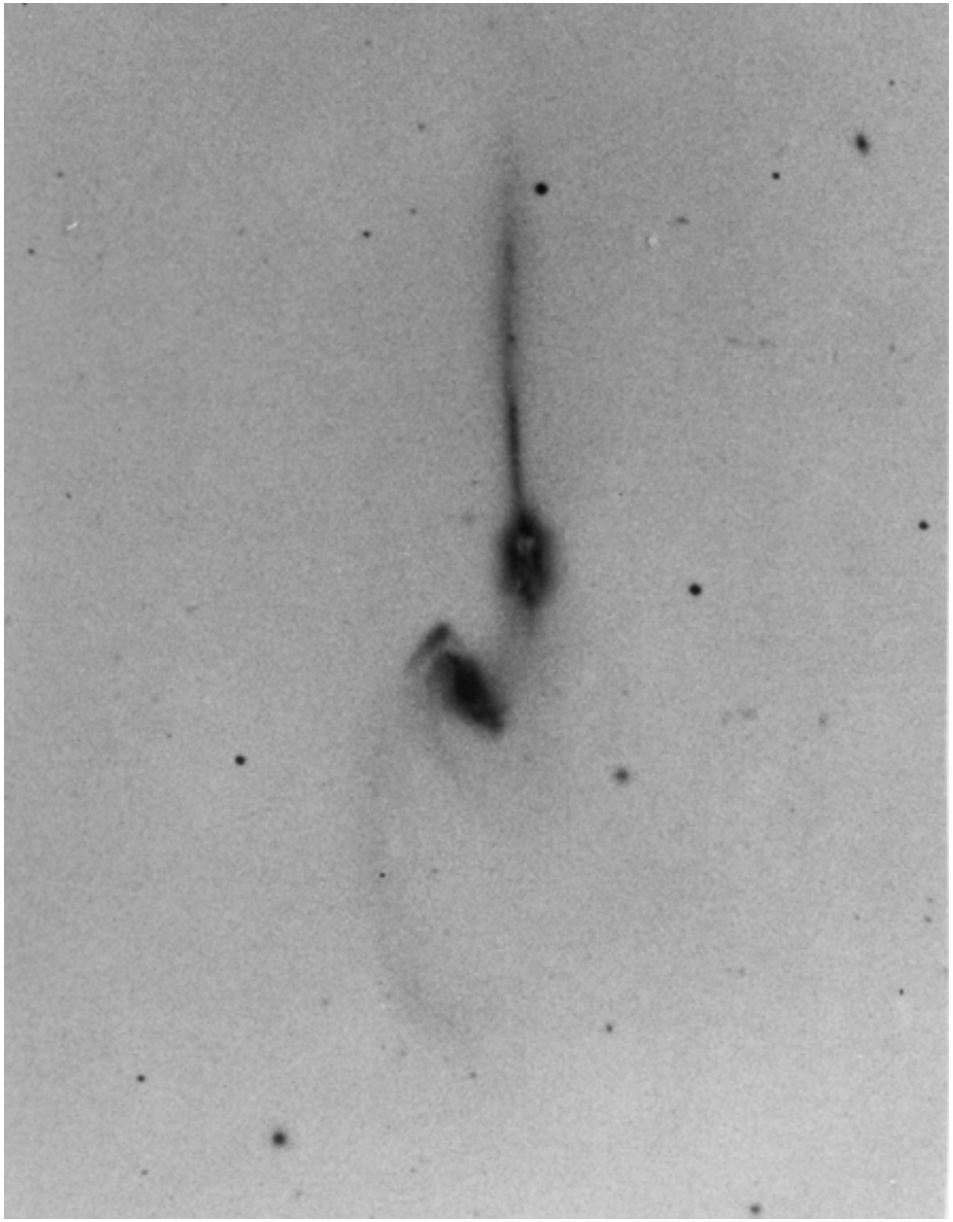

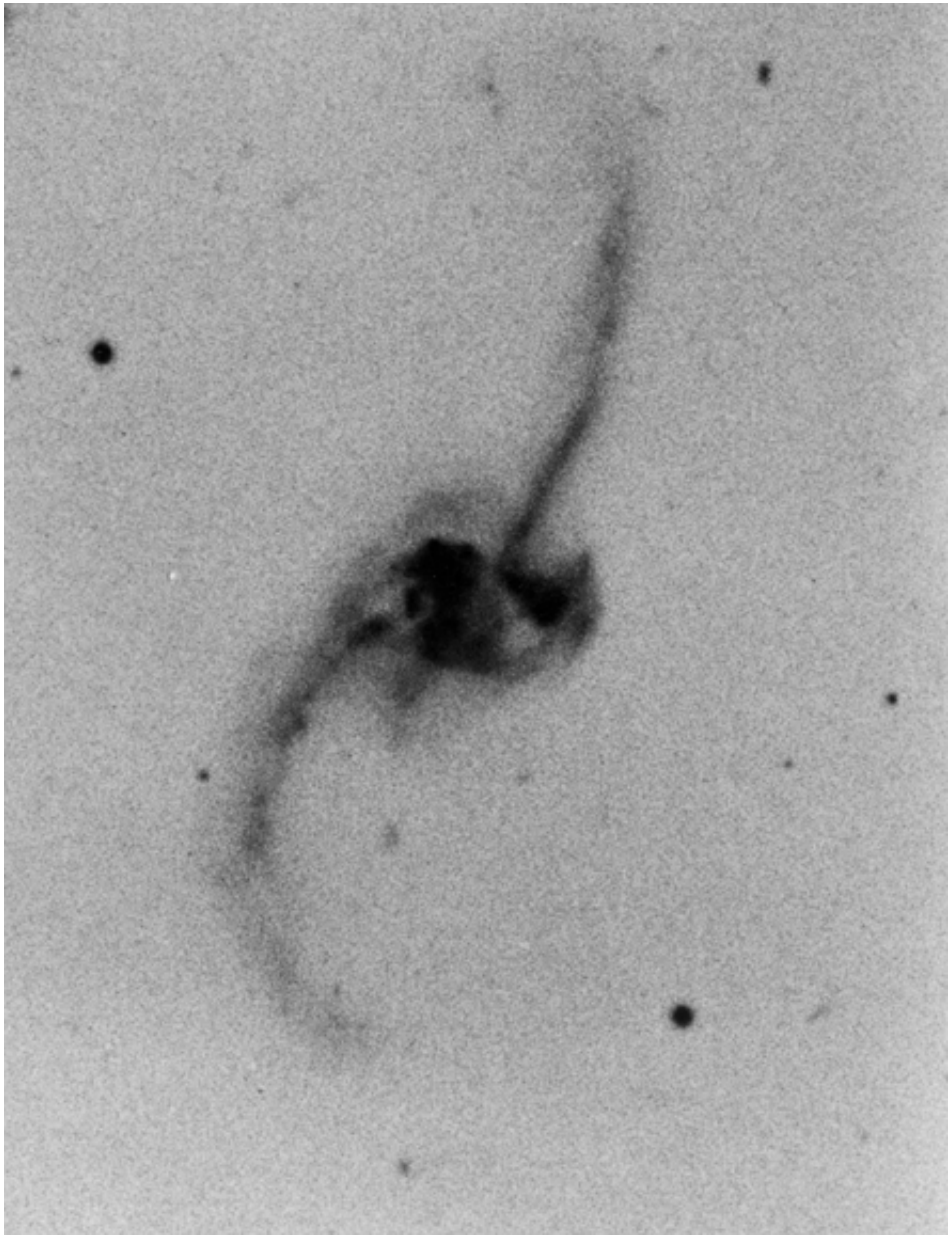

The Mice

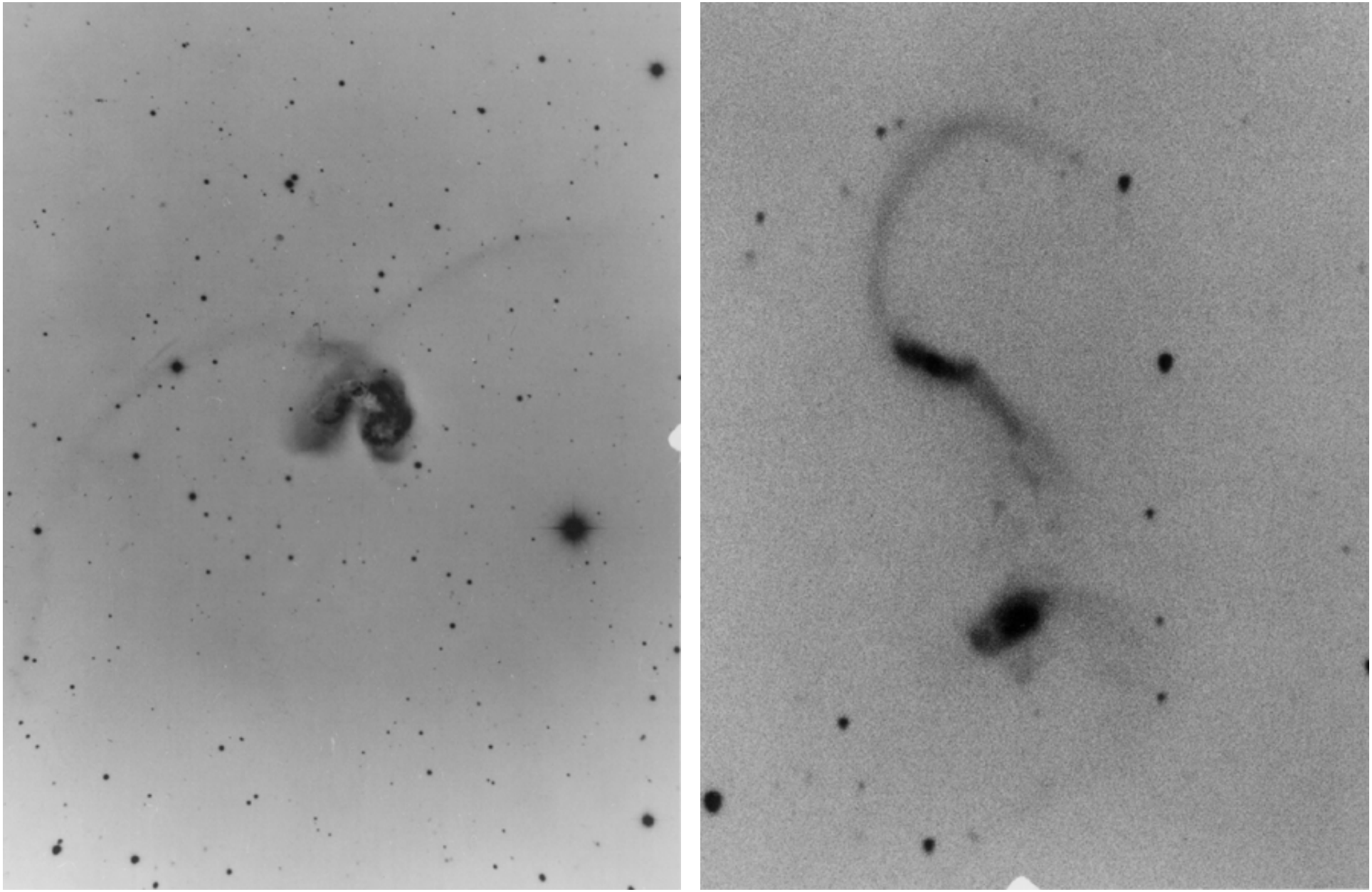

The Antennae

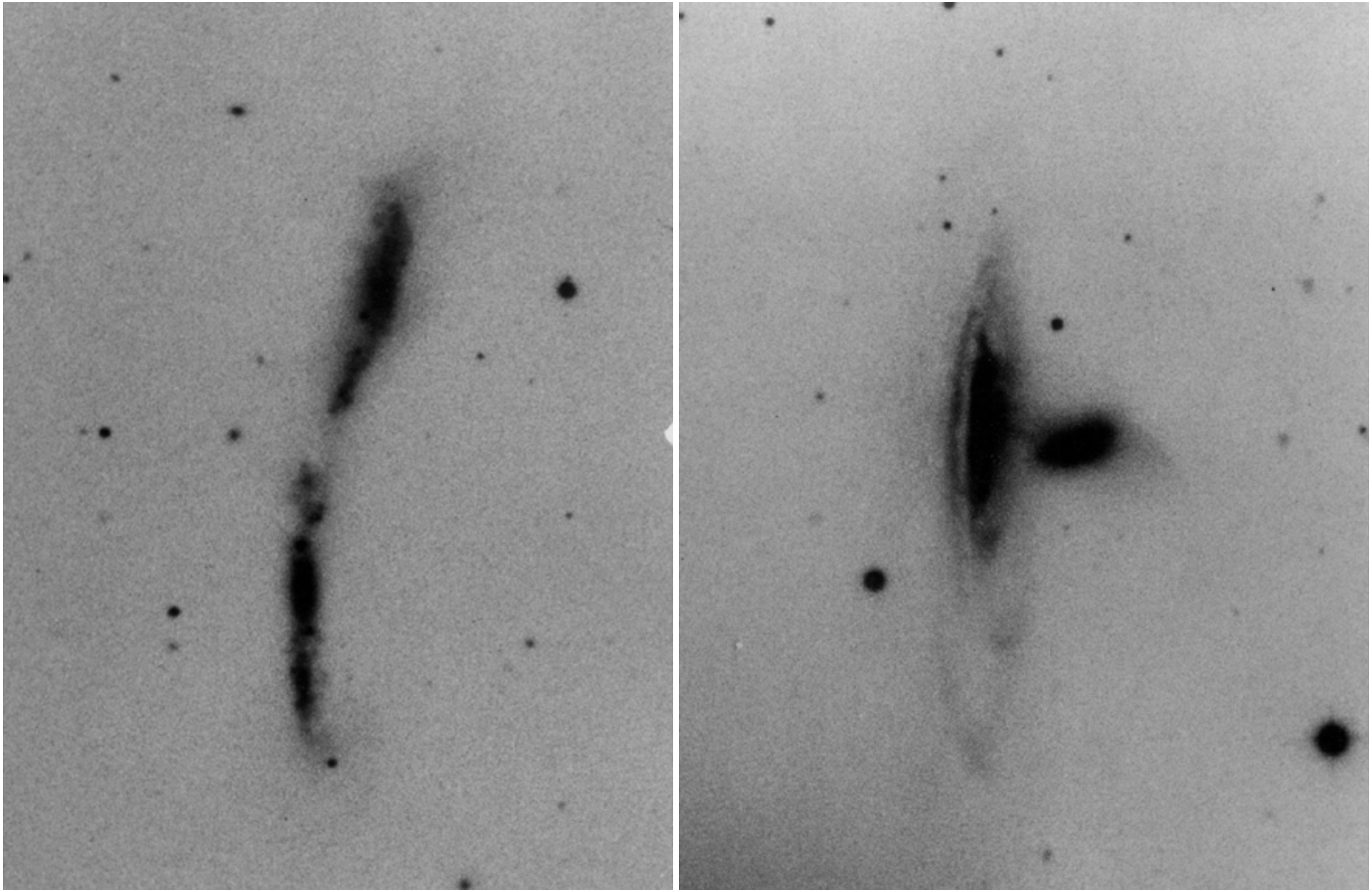

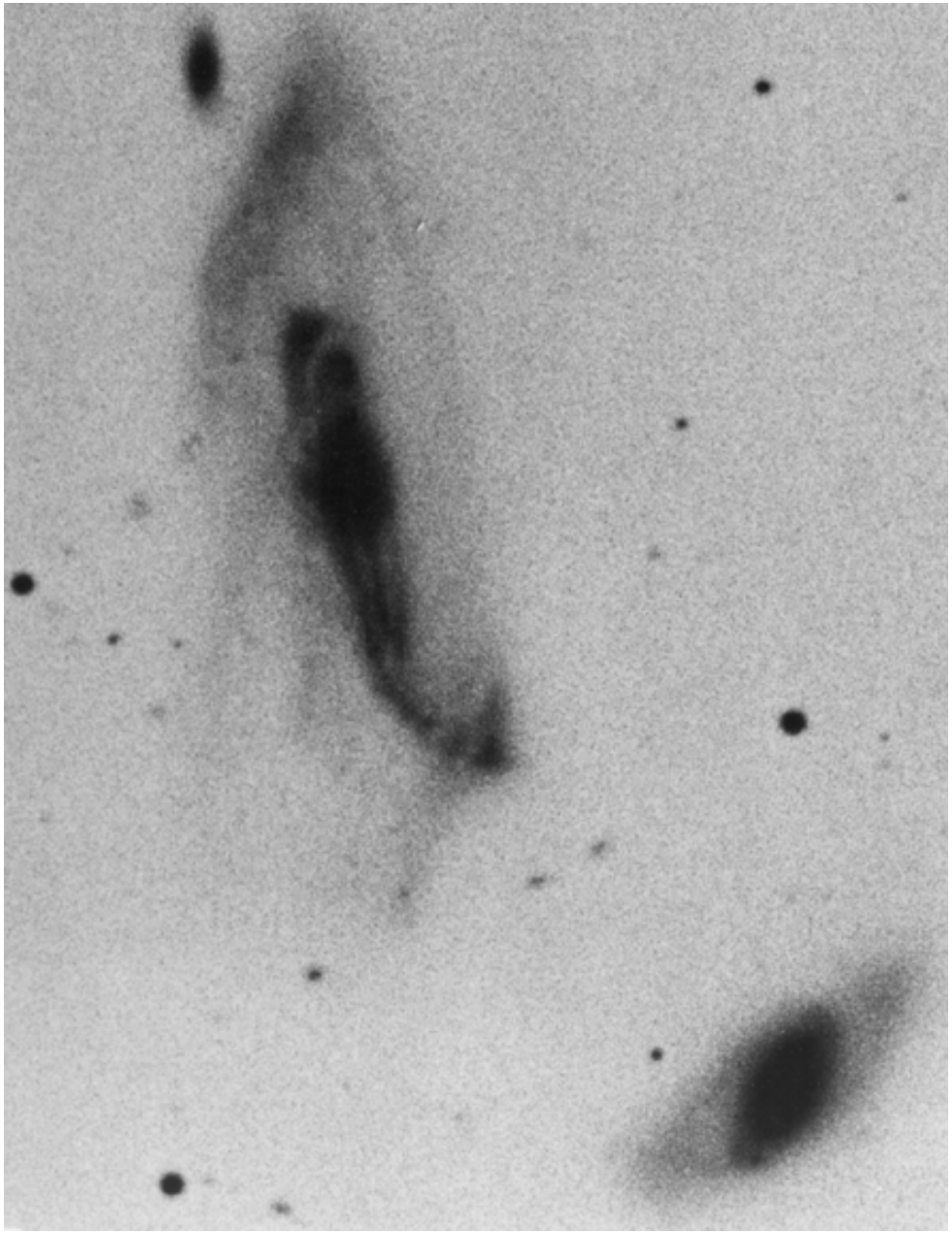

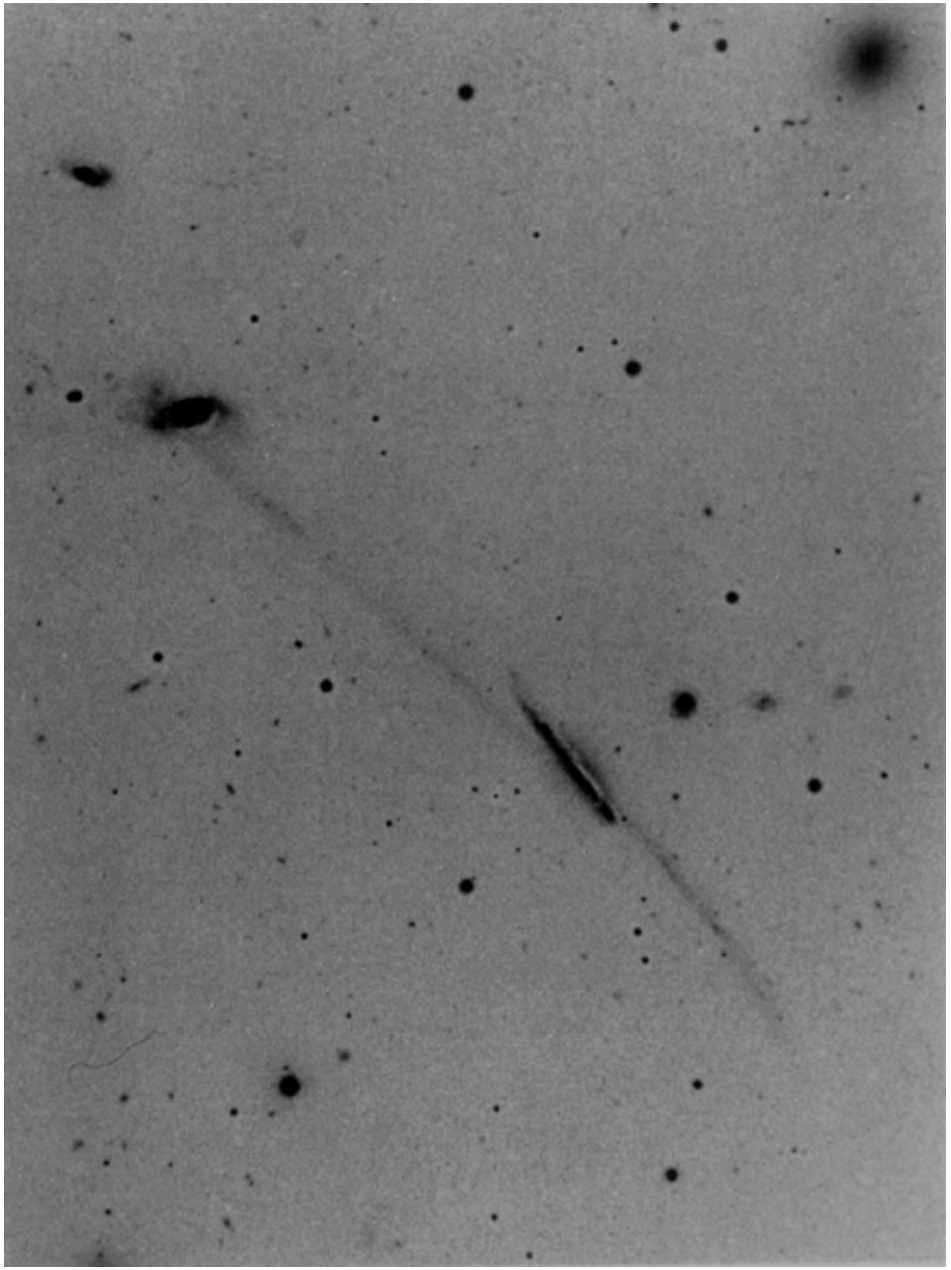

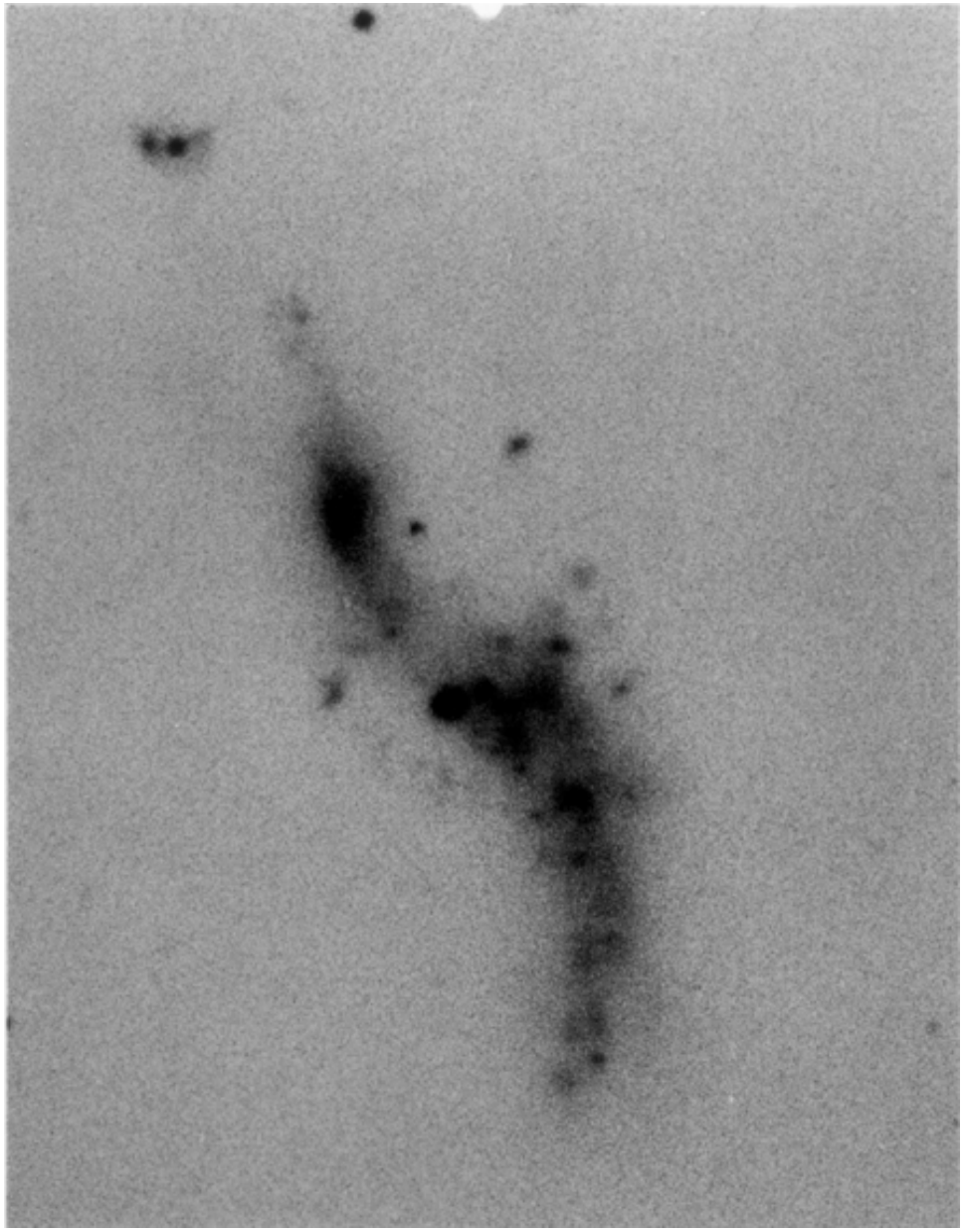

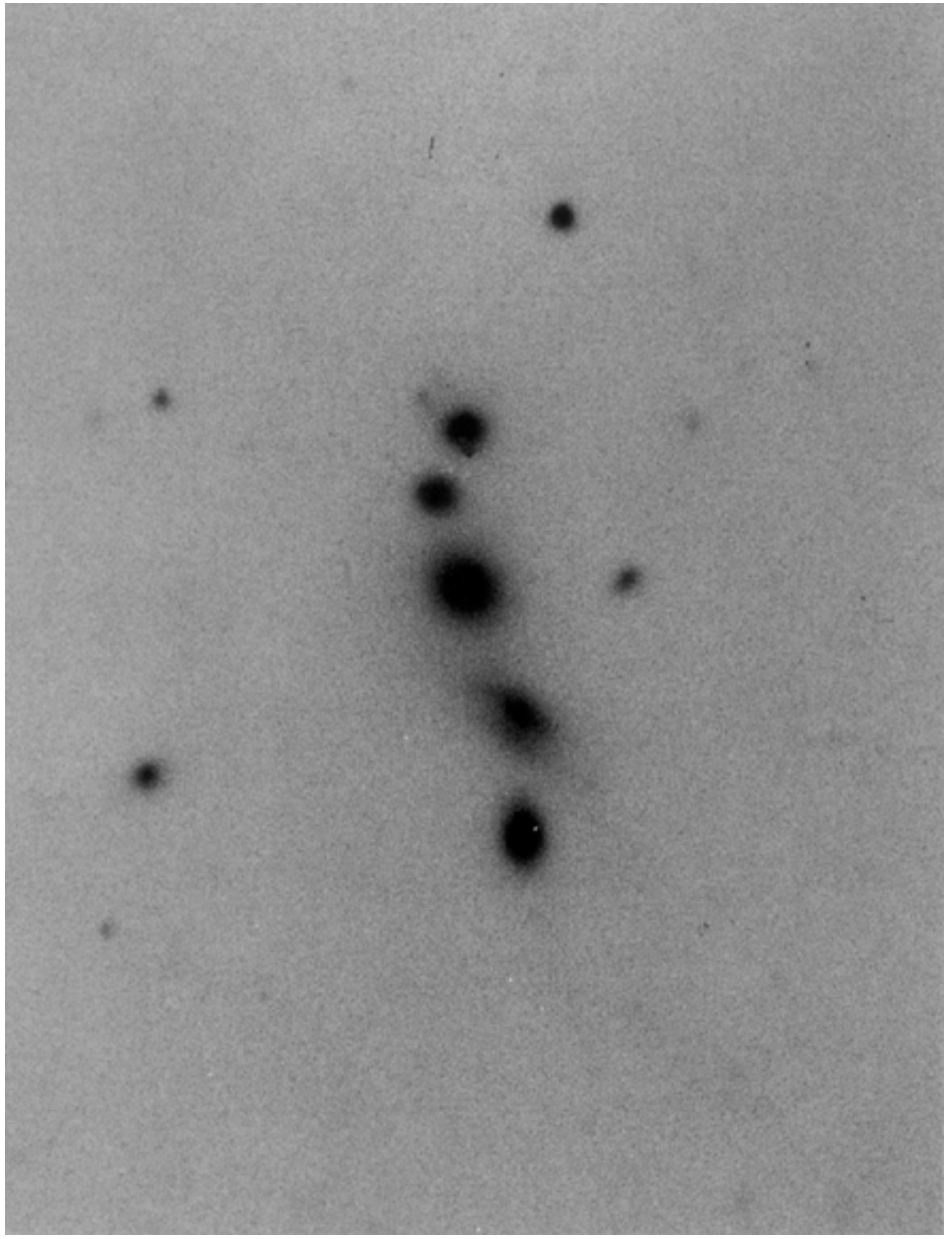

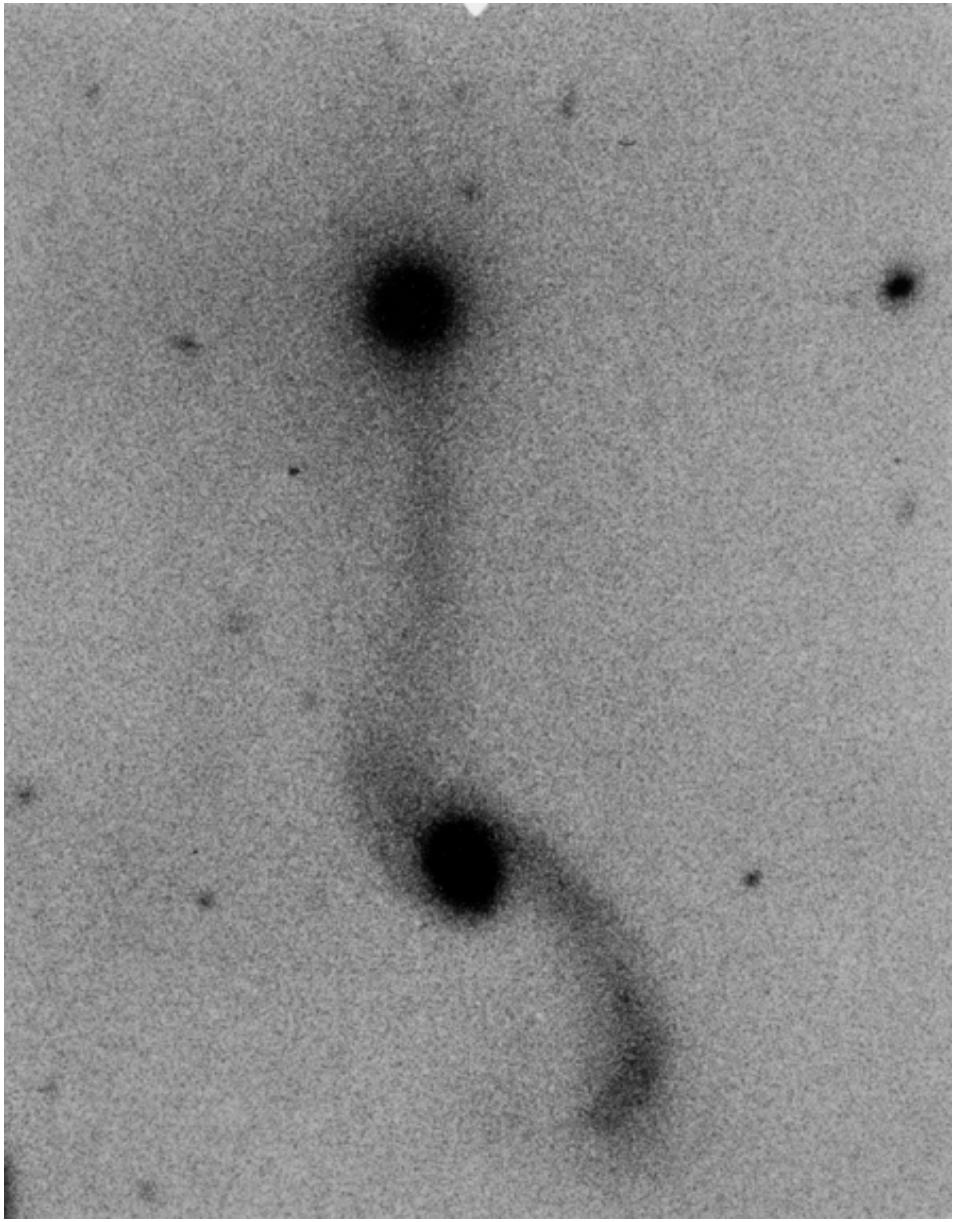

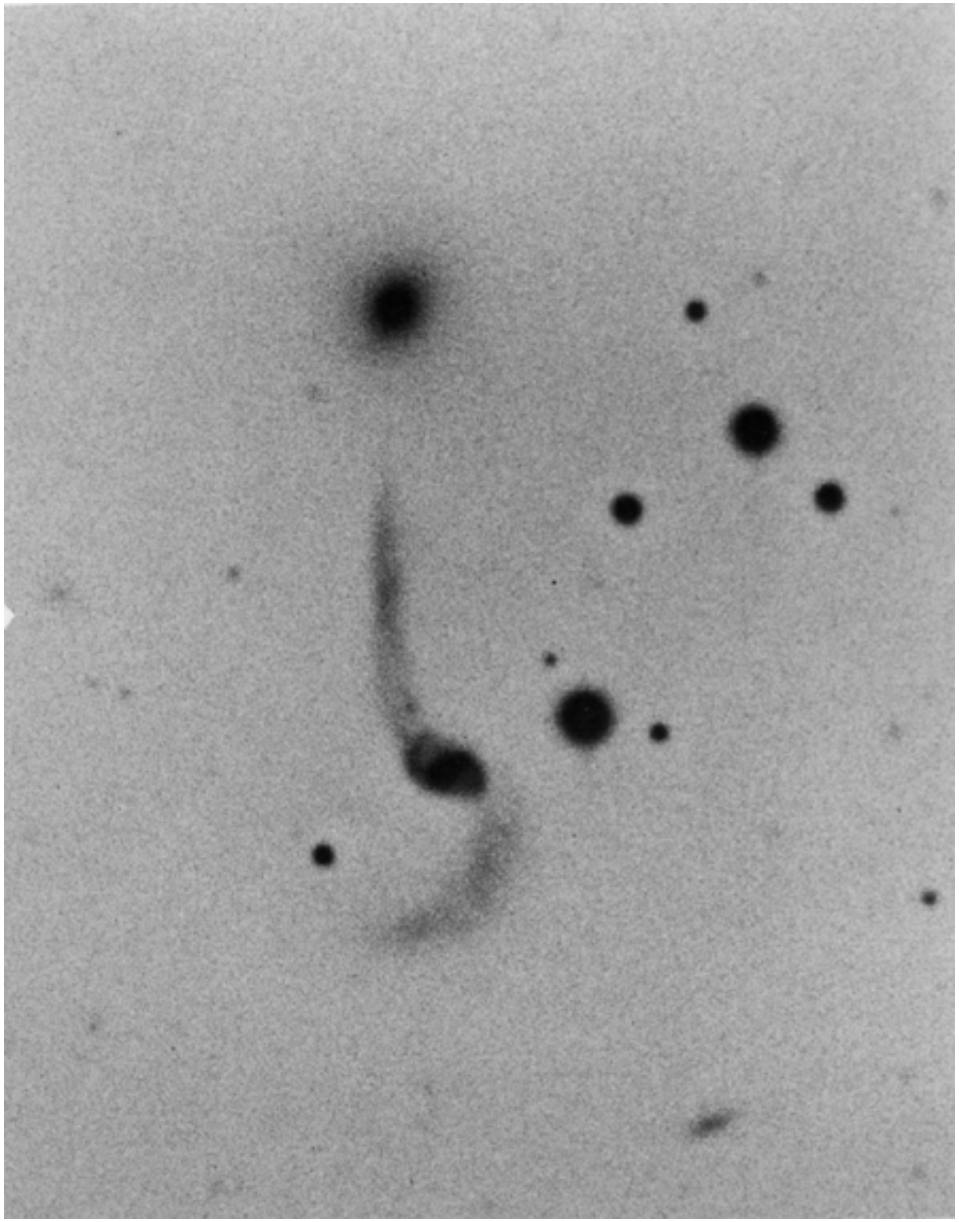

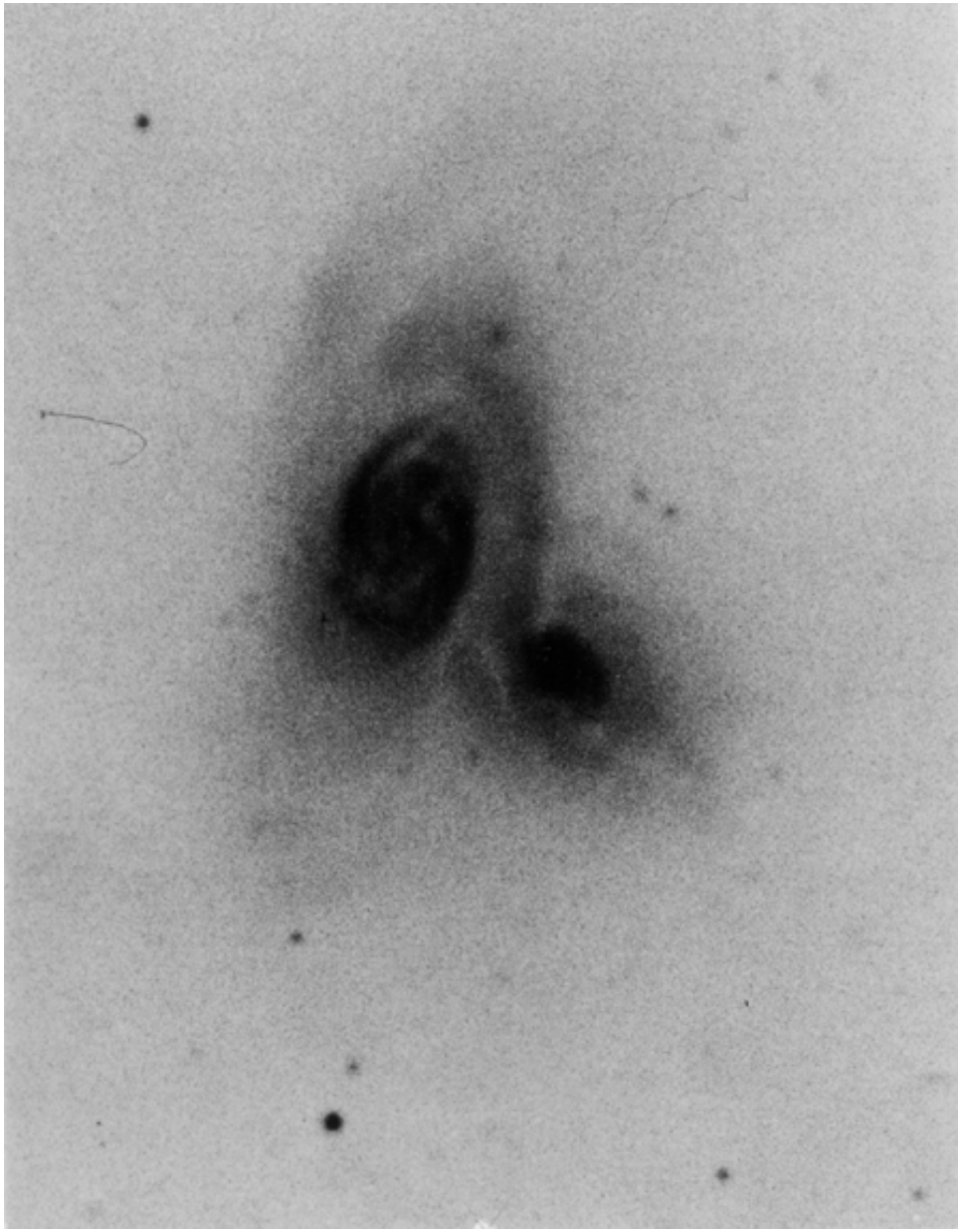

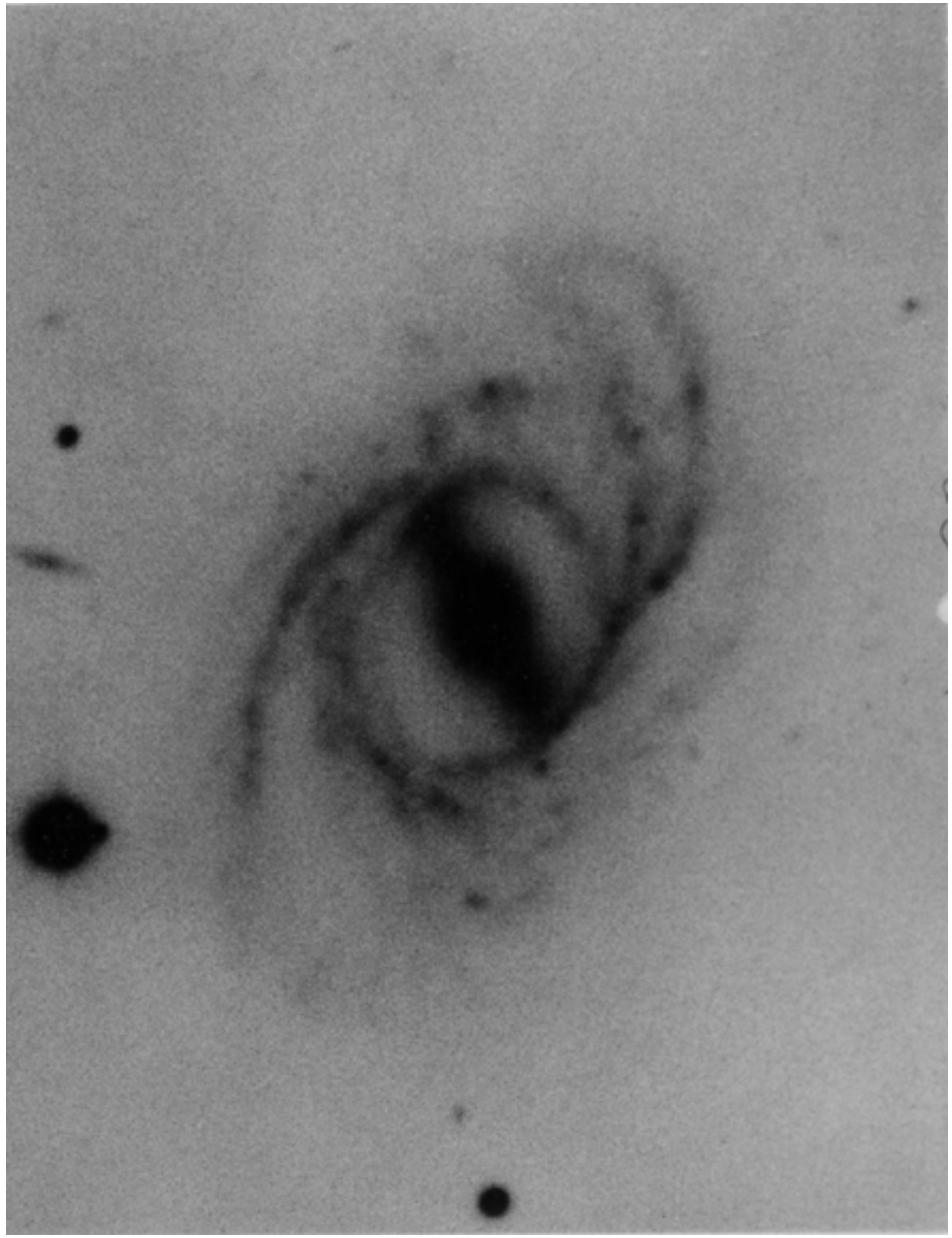

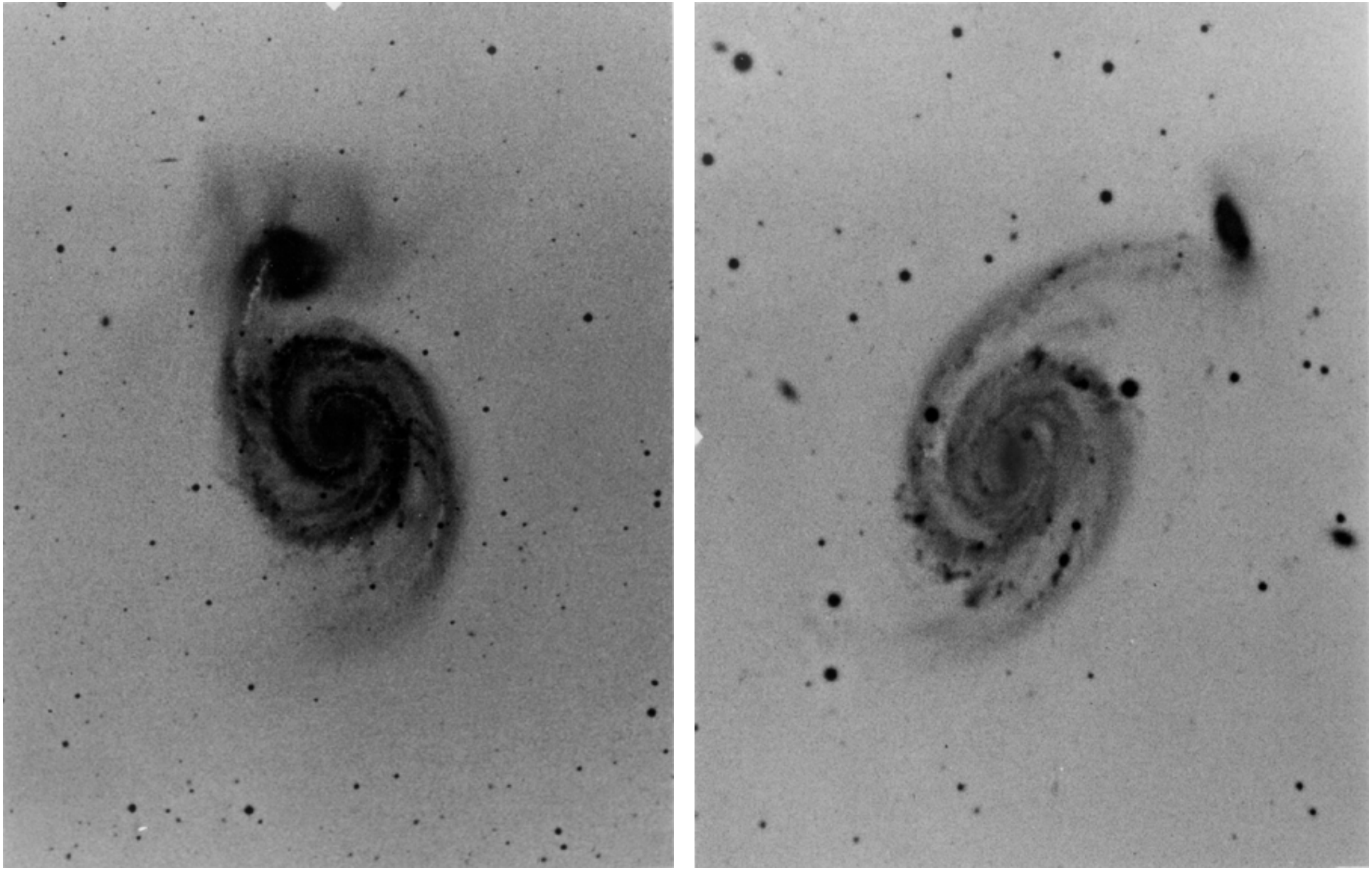

M51

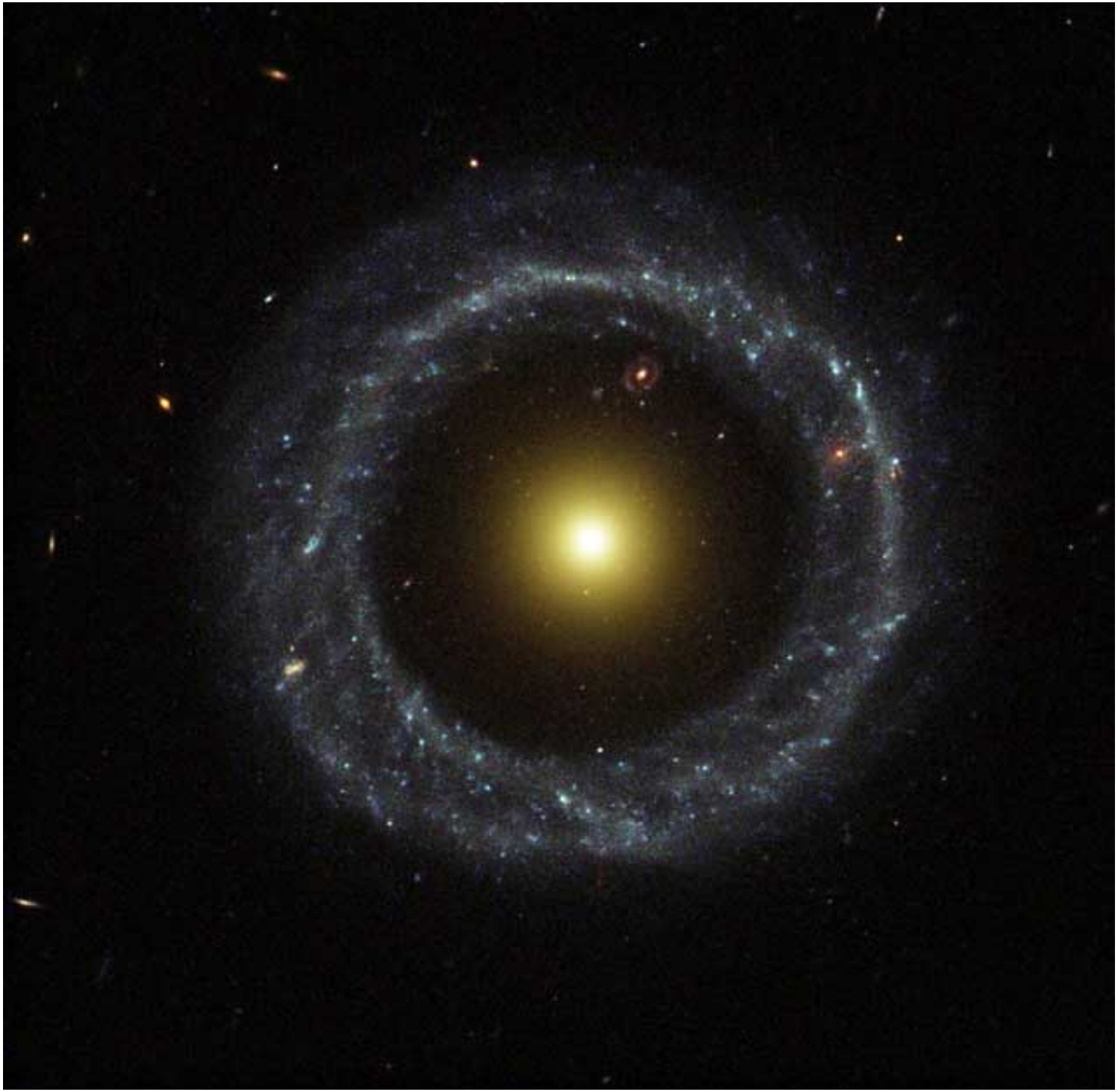

Hoag's object

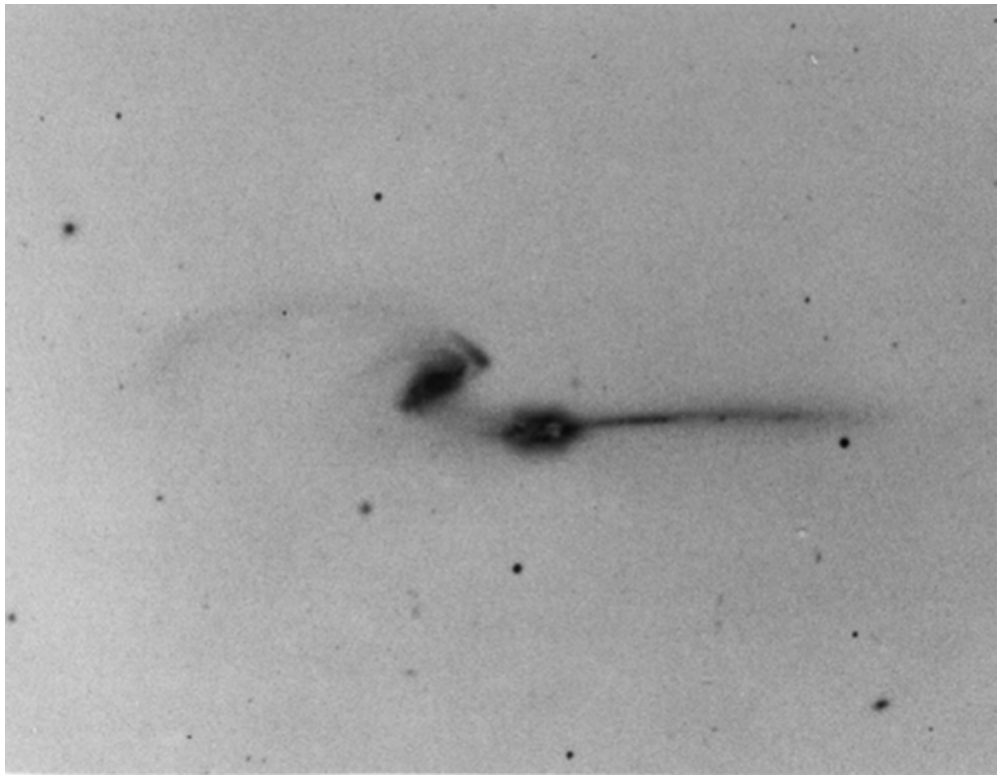

The Mice

model from Toomre & Toomre (1972)

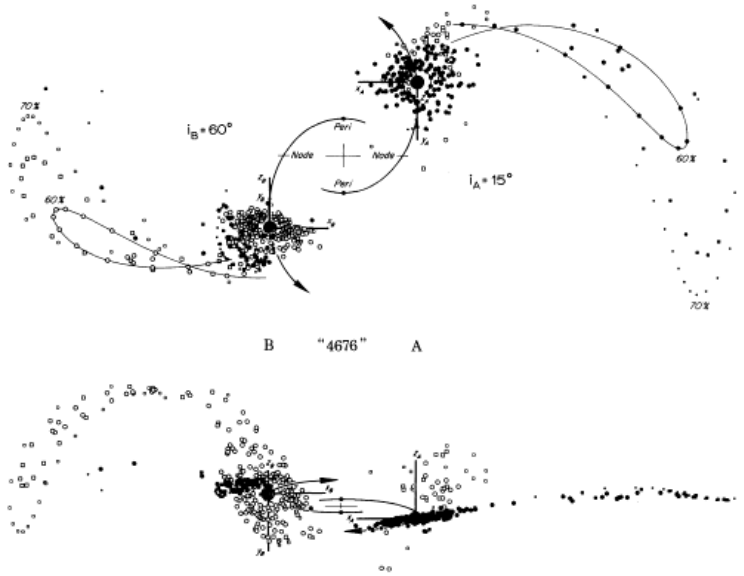

FIG. 22.—Model of NGC 4676. In this reconstruction, two equal disks of radius $0.7R_{min}$ experienced an $e = 0.6$ elliptic encounter, having begun flat and circular at the time $t = -16.4$ of the last apocenter. As viewed from either disk, the adopted node-to-peri angles $\omega_A = \omega_B = -90°$ were identical, but the inclinations differed considerably: $i_A = 15°$, $i_B = 60°$. The resulting composite object at $t = 6.086$ (cf. fig. 18) is shown projected onto the orbit plane in the upper diagram. It is viewed nearly edge-on to the same—from $\lambda_A = 180°$, $\beta_A = 85°$ or $\lambda_B = 0°$, $\beta_B = 160°$—in the lower diagram meant to simulate our actual view of that pair of galaxies. The filled and open symbols distinguish particles originally from disks A and B, respectively.

rather than elaborate, we chose the masses and loadings to be identical, did the same with the simple $\omega_A = \omega_B = -90°$, picked the round values $i_A = 15°$, $i_B = 60°$, chose the viewing longitude to be simply along the line of pericenters, and retained both the eccentricity and the 135° viewing time already used in figure 18. Thus the B object in figure 22 is virtually an "off-the-shelf" item. It differs from its predecessor in figure 18 only in the coding of certain of its particles, the display of its not-too-offensive accretion cloud above mass A, and a 45° more advanced longitude and 10° different latitude of viewing.

One almost incidental advantage of the present model is that, like the real tail A, ours looks slightly concave downward—or toward the west. More important is its agreement with the rough sense of the velocities measured in hulk B by the Burbidges: although our remnant B lacks the oval outline of the real object, its excess Doppler speeds are likewise positive and negative in the "north" and "south," respectively. (Moreover, the fact that our remnant B happens to be viewed only 20° from face-on cautions that the actual rotation in 4676B could well be twice the observed ± 200 km s^{-1}, and hence also about twice the nominal speeds of our retained test particles. Thus

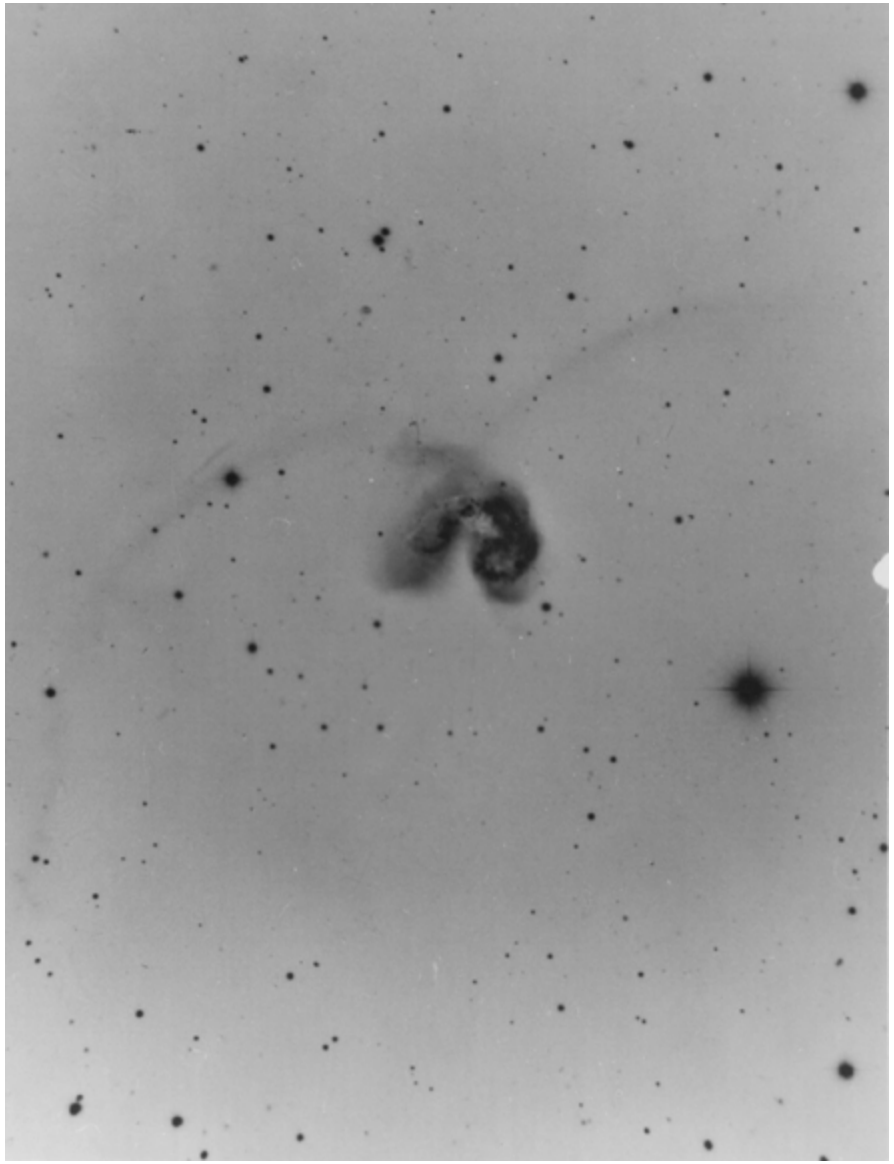

The Antennae

model from Toomre & Toomre (1972)

been concerned whether in fact it was possible to obtain seemingly *crossed* tails from tidal interactions. Figure 23 says we need not have worried.

By using figure 18, it is quite easy in retrospect to grasp the geometric essentials of this construction. Imagine that every bare companion in that ω survey carries an $i = +60°$ tail of its own, each such tail having been chosen from among the present four possibilities simply after a 180° visual rotation about the axis normal to the orbit

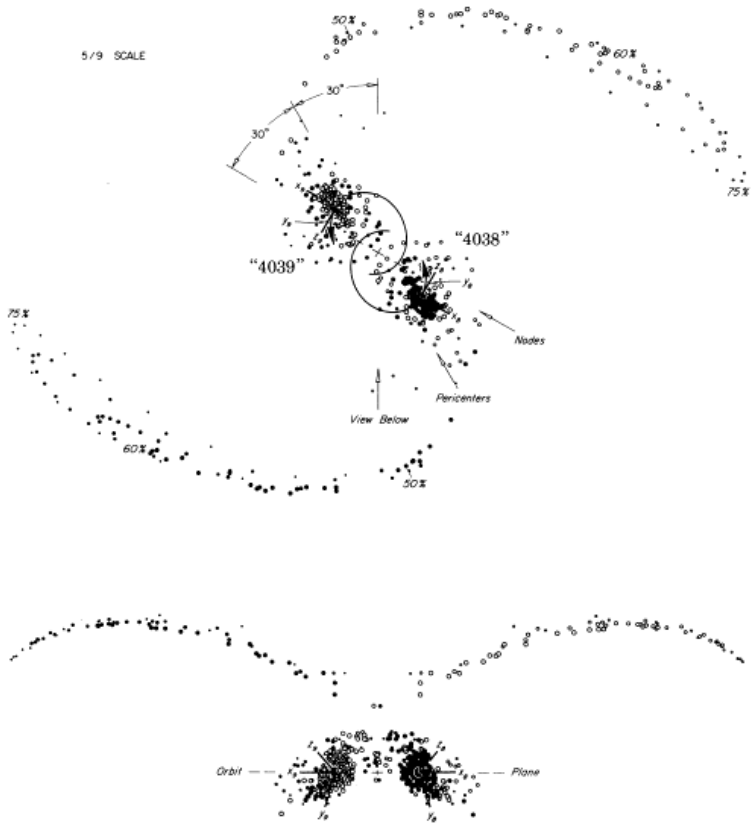

FIG. 23.—Symmetric model of NGC 4038/9. Here two identical disks of radius $0.75R_{\min}$ suffered an $e \approx 0.5$ encounter with orbit angles $i_8 = i_9 = 60°$ and $\omega_8 = \omega_9 = -30°$ that appeared the same to both. The above all-inclusive views of the debris and remnants of these disks have been drawn exactly normal and edge-on to the orbit plane; the latter viewing direction is itself 30° from the line connecting the two pericenters. The viewing time is $t = 15$, or slightly past apocenter. The filled and open symbols again disclose the original loyalties of the various test particles.

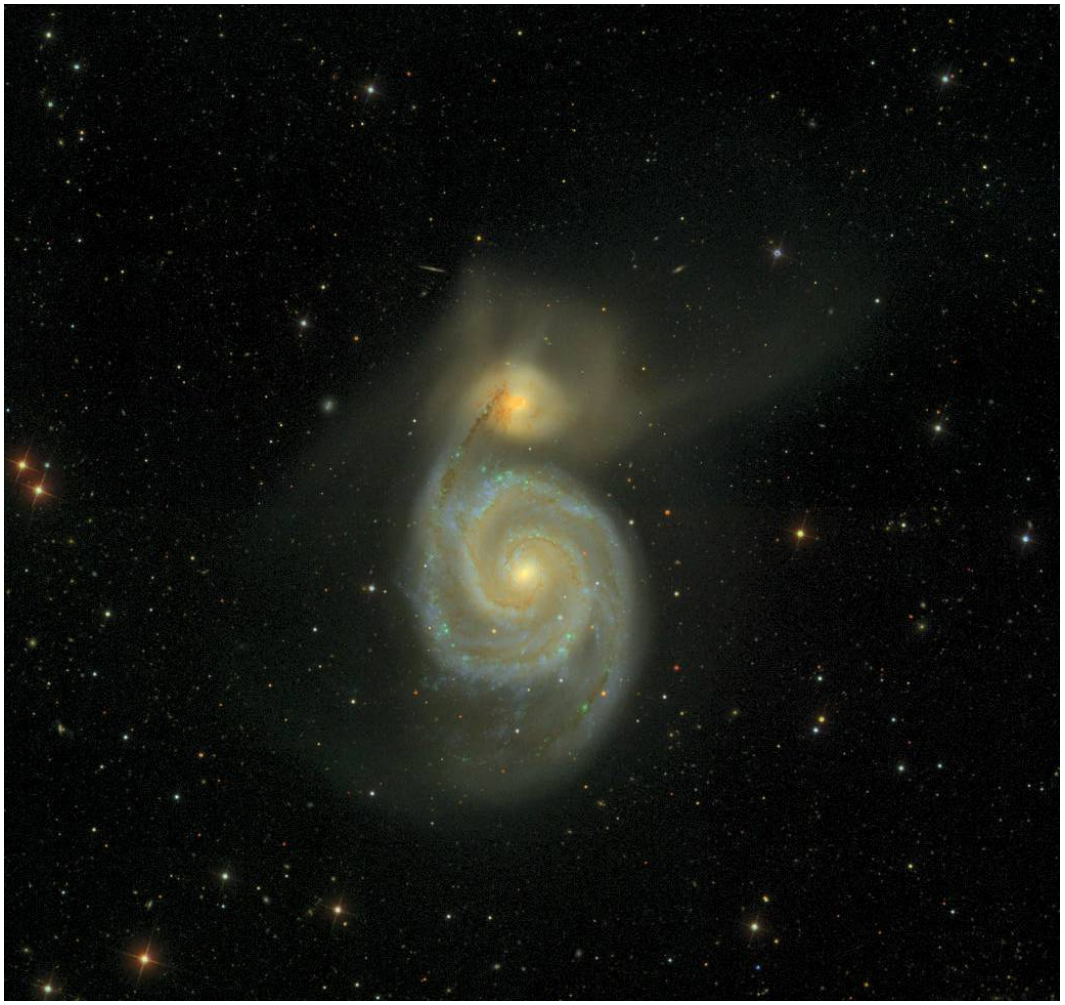

M51

model from Toomre & Toomre (1972)

at about that radius. It consists of two parts: One, of course, is the bridgelike northern arm which a number of observers (cf. Roberts and Warren 1970) have already felt partly obscures the companion. The other is the *broad*, curving, fainter counterarm to the south and southwest of the main disk. Though this second major clue is scarcely visible in the *Hubble Atlas* (Sandage 1961), it is very evident in the deeper *Sky Survey* and Arp 85 photographs and unmistakable in the IIIaJ exposure by van den Bergh (1969). Together with the projected position and excess line-of-sight velocity of the companion, it is these two features—and they alone—that comprised the prime goals of our reconstruction of the encounter shown in figures 20 and 21.

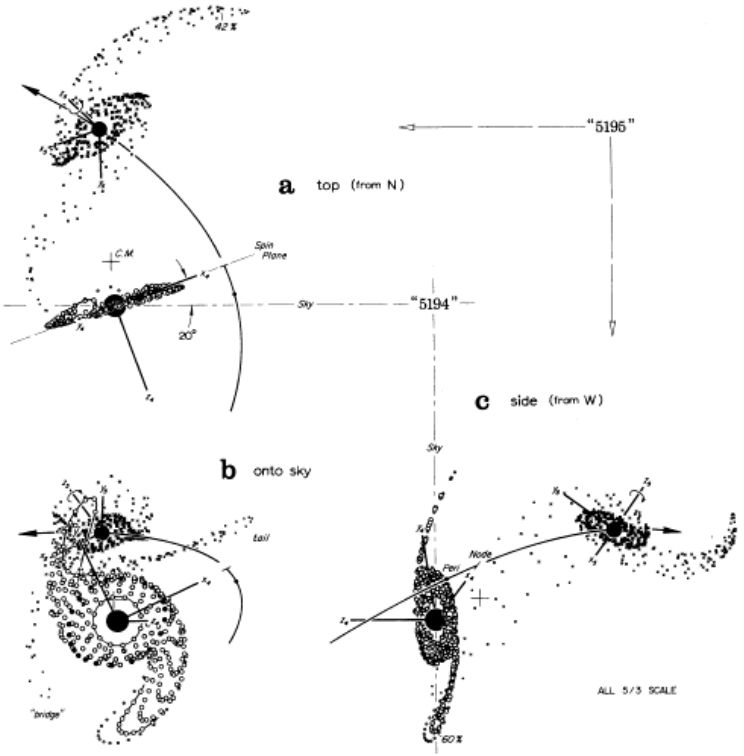

FIG. 21.—Model of the recent encounter between M51 and NGC 5195. Shown here at $t = 2.4$ are three mutually orthogonal views of the consequences of a highly elliptic $e = 0.8$ passage of a supposedly disklike "5195." This satellite was chosen to be one-third as massive, and of exactly 0.7 times the linear dimensions, of the "5194" primary—which itself contains particles from initial radii $0.2(0.05)0.4(0.033)0.633 R_{min}$. The orbit plane differs by an angle $i_4 = -70°$ from the initial spin plane of the larger disk and by $i_5 = -60°$ from that of the smaller; however, the arguments $\omega_4 = \omega_5 = -15°$ of the pericenters were here kept identical, to make the above nodal axes x_4 and x_5 exactly antiparallel. The three views show the combined system as it would appear not only (*b*) to us ($\lambda_4 = 65°$, $\beta_4 = -20°$), but also edge-on to our sky from (*a*) the "north" ($-25°$, 90°) and (*c*) the "west" (65°, 70°) directions.

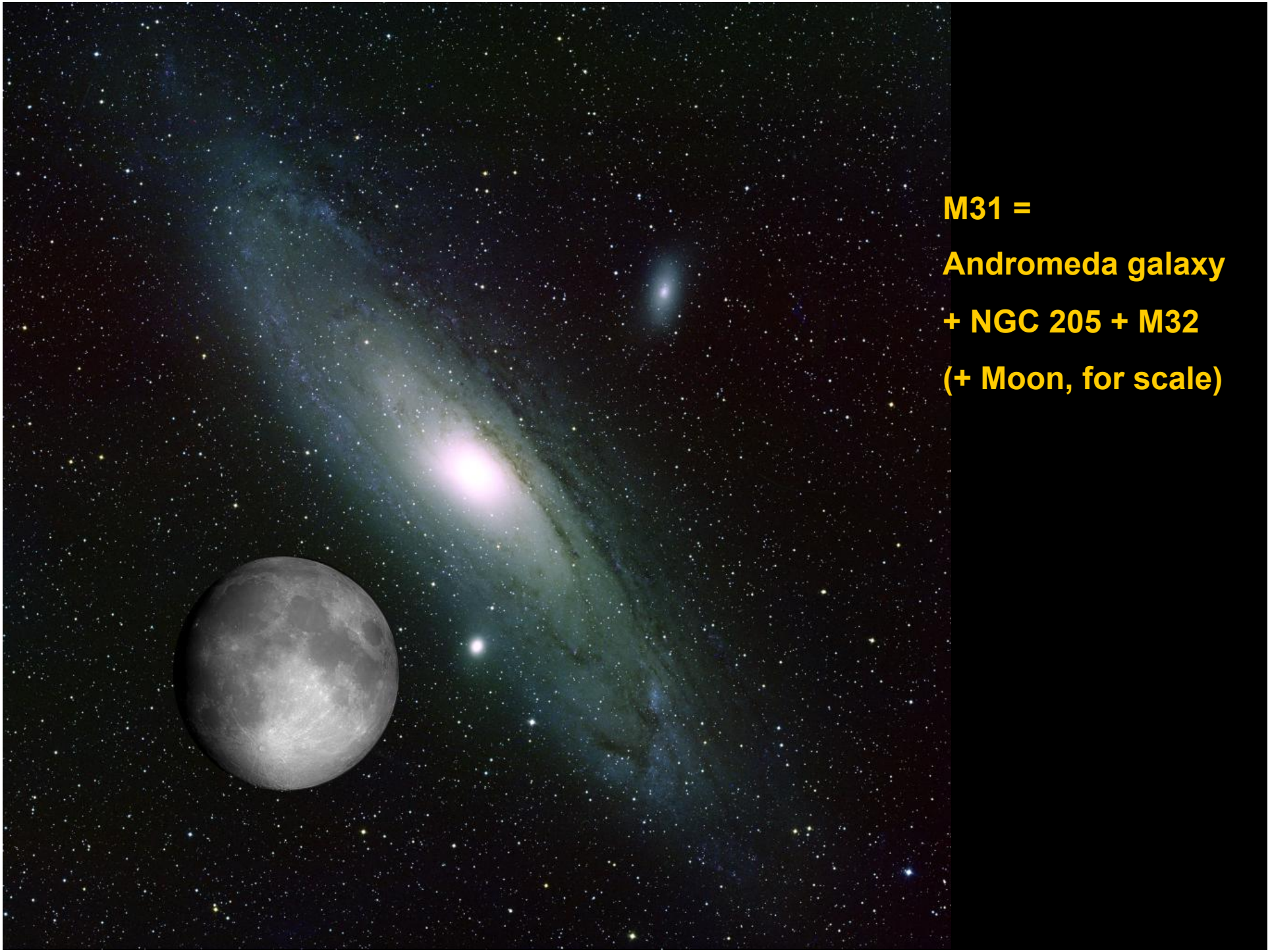
M31 =
Andromeda galaxy
+ NGC 205 + M32
(+ Moon, for scale)

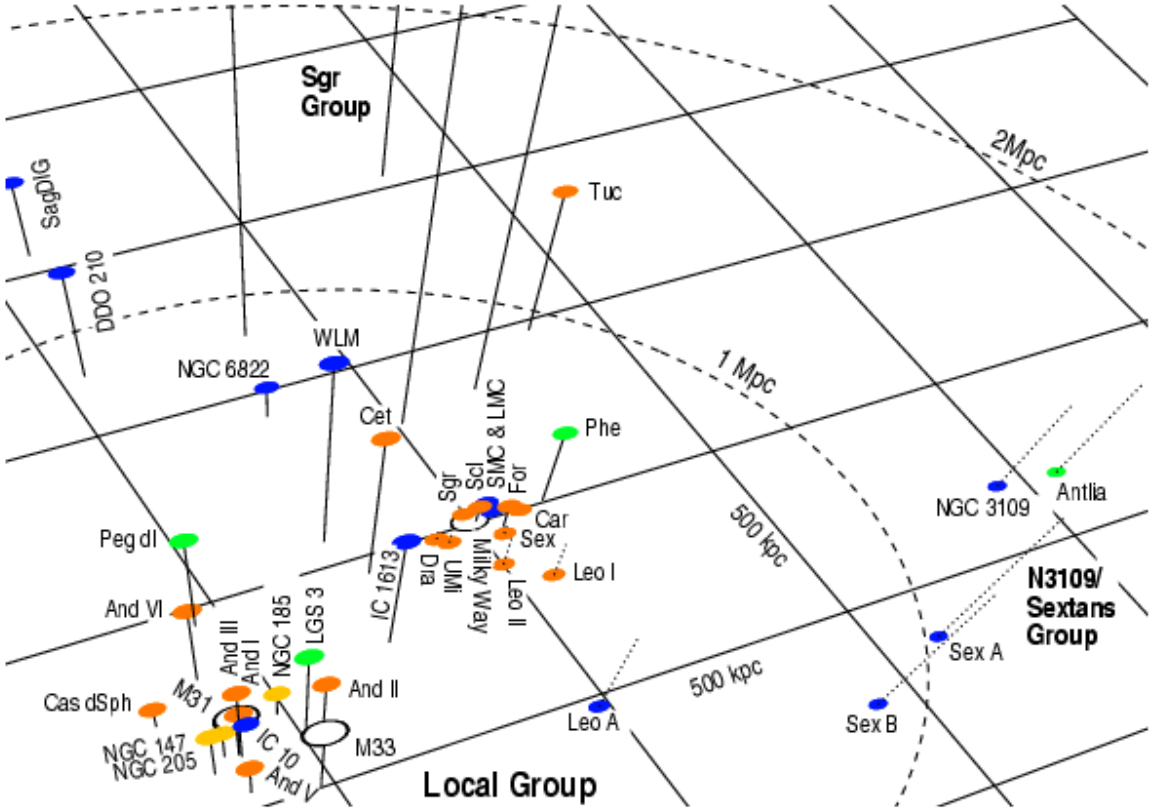

Figure 1. A scaled 3-D representation of the Local Group (LG). The dashed ellipsoid marks a radius of 1 Mpc around the LG barycenter (assumed to be at 462 kpc toward $l = 121.7$ and $b = -21.3$ following Courteau & van den Bergh 1999). Distances of galaxies from the the arbitrarily chosen plane through the Milky Way are indicated by solid lines (above the plane) and dotted lines (below). Morphological segregation is evident: The dEs and gas-deficient dSphs (light symbols) are closely concentrated around the large spirals (open symbols). DSph/dIrr transition types (e.g., Pegasus, LGS 3, Phoenix) tend to be somewhat more distant. Most dIrrs (dark symbols) are fairly isolated and located at larger distances. Also indicated are the locations of two nearby groups.

Grebel (2000)


Magellanic
clouds

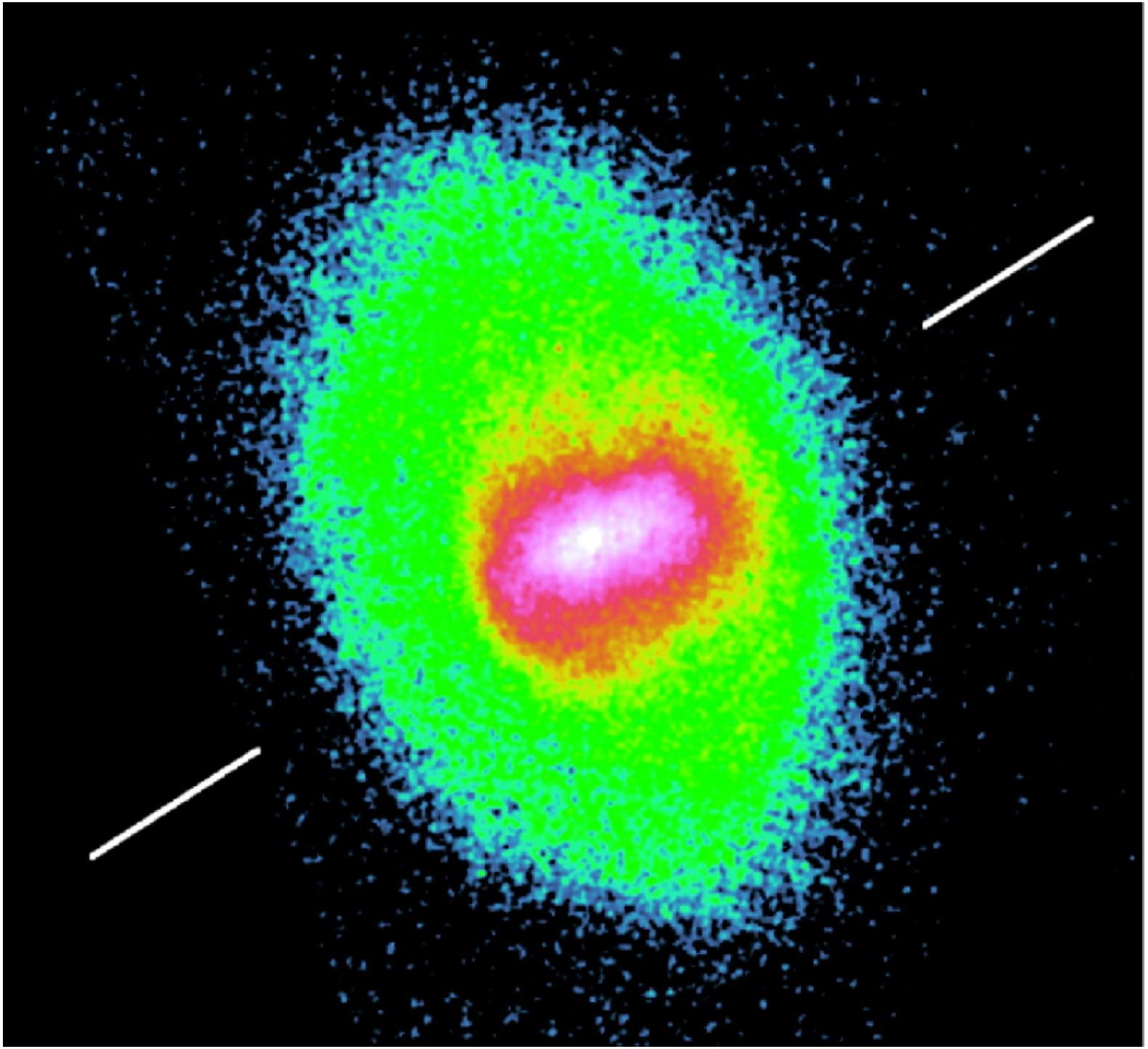

van der
Marel (2002)

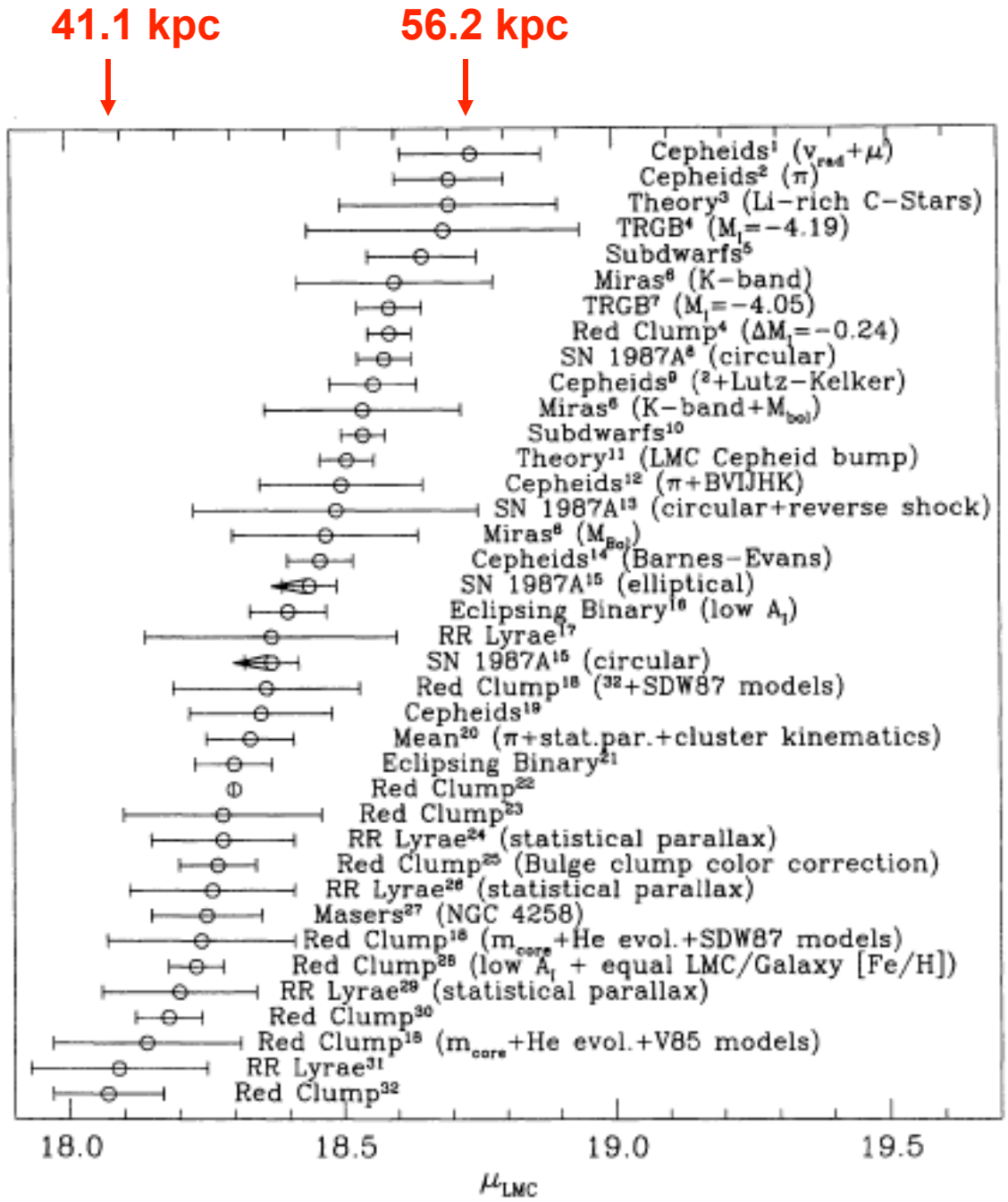
41.1 kpc
56.2 kpc
Cepheids[1] ($v_{rad}+\mu$)
Cepheids[2] (π)
Theory[3] (Li-rich C-Stars)
TRGB[4] ($M_I=-4.19$)
Subdwarfs[5]
Miras[6] (K-band)
TRGB[7] ($M_I=-4.05$)
Red Clump[4] ($\Delta M_I=-0.24$)
SN 1987A[8] (circular)
Cepheids[9] (^{2}+Lutz-Kelker)
Miras[6] (K-band+M_{bol})
Subdwarfs[10]
Theory[11] (LMC Cepheid bump)
Cepheids[12] (π+BVIJHK)
SN 1987A[13] (circular+reverse shock)
Miras[6] (M_{Bol})
Cepheids[14] (Barnes-Evans)
SN 1987A[15] (elliptical)
Eclipsing Binary[16] (low A_I)
RR Lyrae[17]
SN 1987A[15] (circular)
Red Clump[18] (^{32}+SDW87 models)
Cepheids[19]
Mean[20] (π+stat.par.+cluster kinematics)
Eclipsing Binary[21]
Red Clump[22]
Red Clump[23]
RR Lyrae[24] (statistical parallax)
Red Clump[25] (Bulge clump color correction)
RR Lyrae[26] (statistical parallax)
Masers[27] (NGC 4258)
Red Clump[18] (m_{core}+He evol.+SDW87 models)
Red Clump[28] (low A_I + equal LMC/Galaxy [Fe/H])
RR Lyrae[29] (statistical parallax)
Red Clump[30]
Red Clump[18] (m_{core}+He evol.+V85 models)
RR Lyrae[31]
Red Clump[32]
18.0
18.5
19.0
19.5
μ_{LMC}

Gibson (1999)

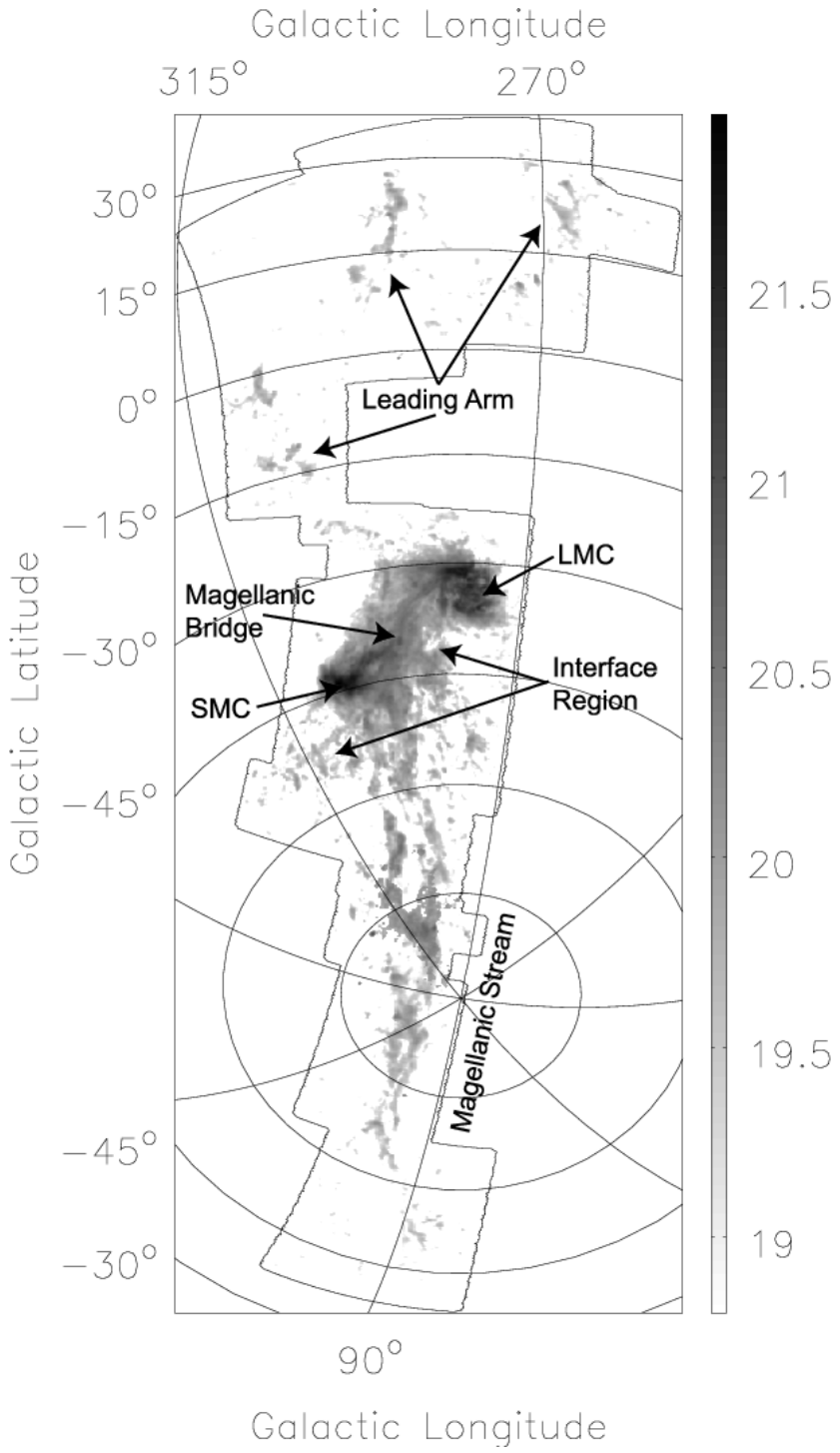

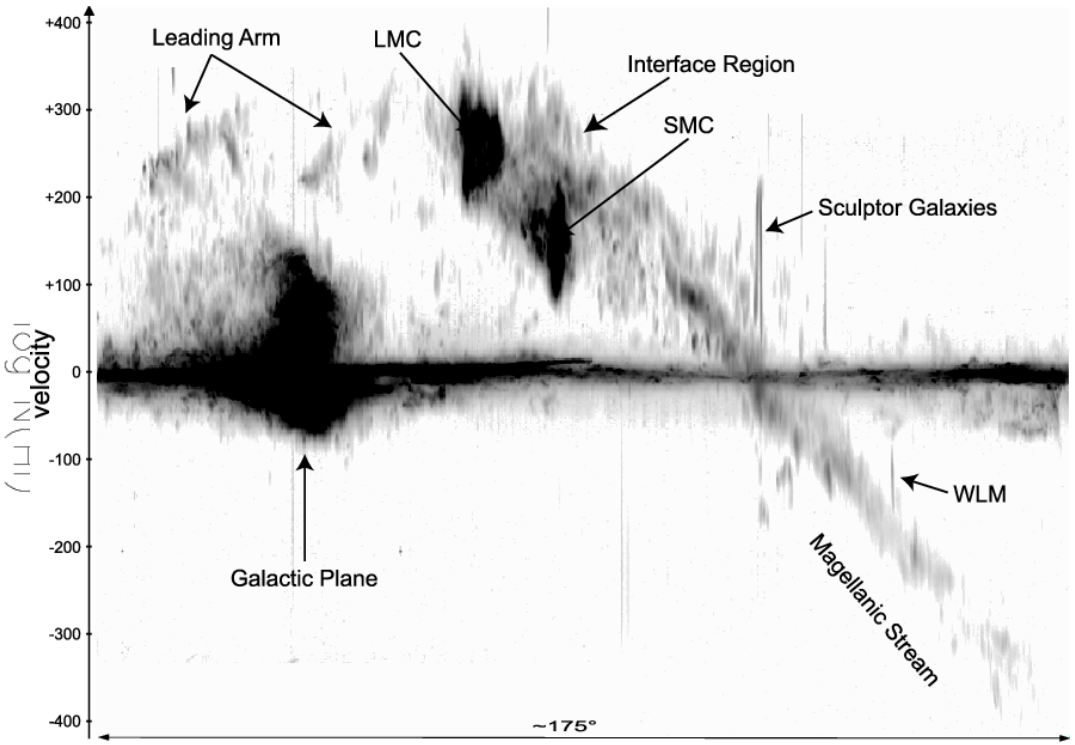

Bruns et al. (2005)

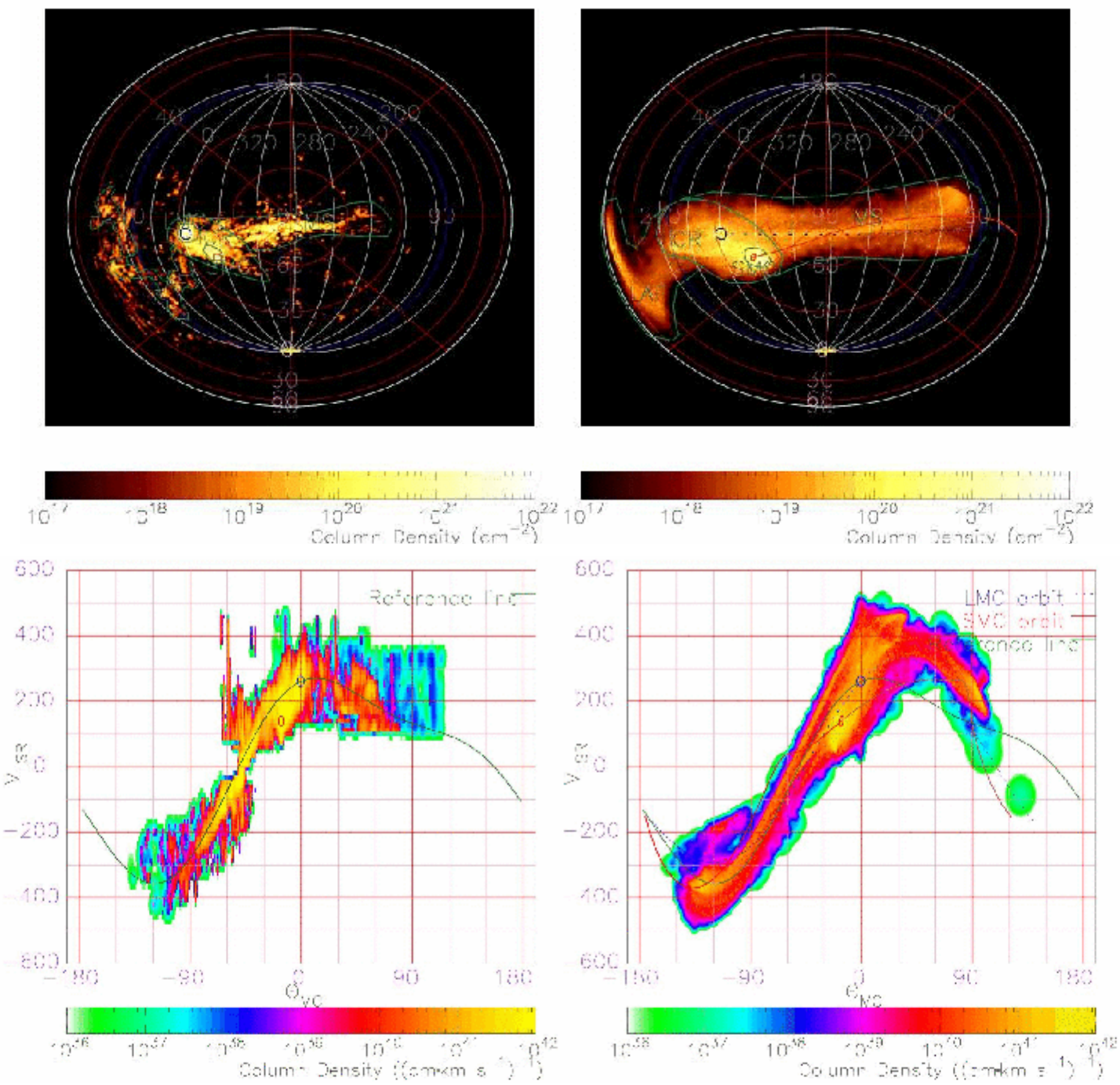

Connors et al. (2005)

Fornax dwarf galaxy

Leo I dwarf galaxy


Pegasus dwarf spheroidal galaxy
1,000 light years
Keck 10 meter telescope / Grebel & Guhathakurta

Ursa Minor dwarf galaxy (dSph)

Draco dwarf galaxy (dSph)

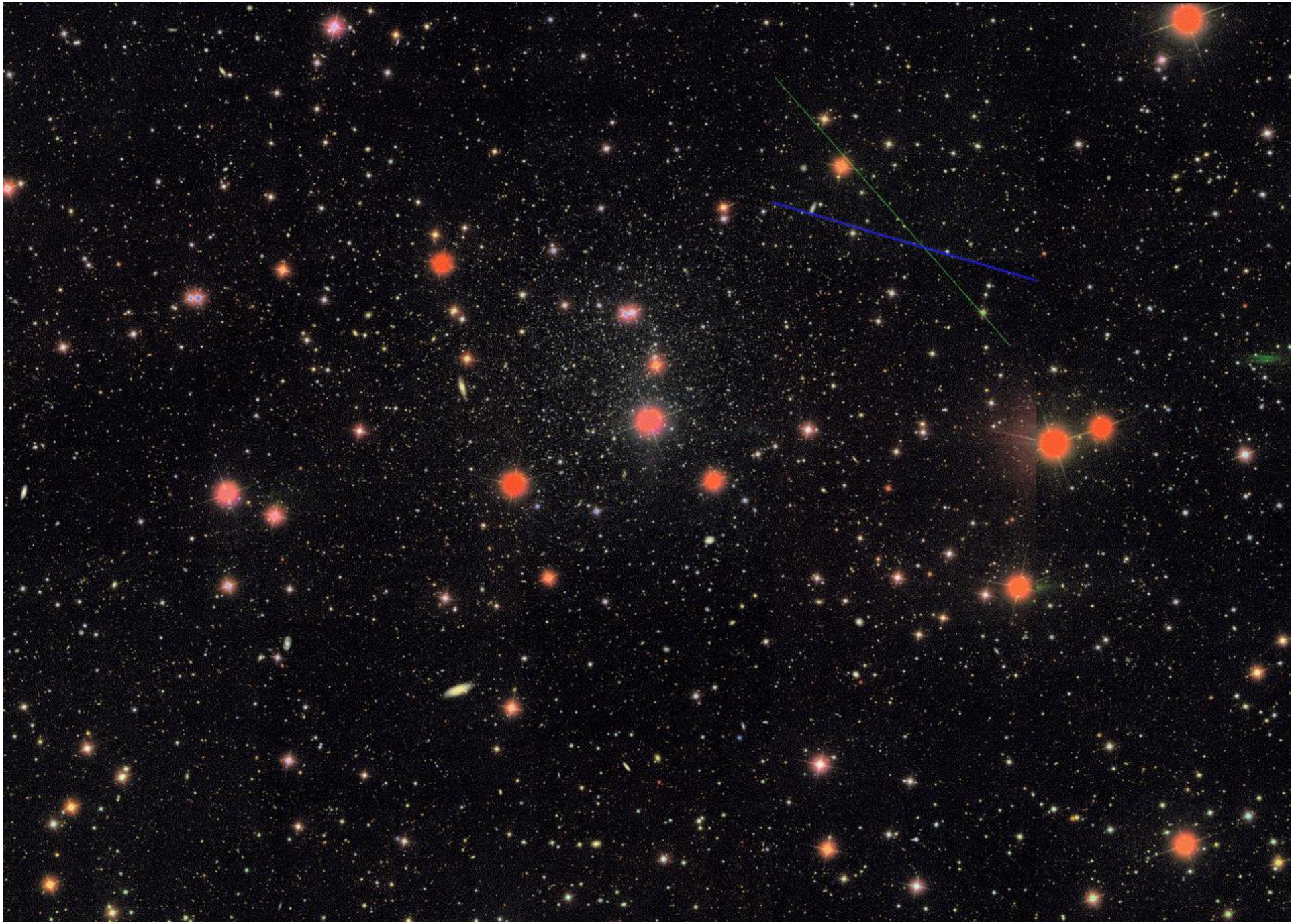

Draco dwarf galaxy

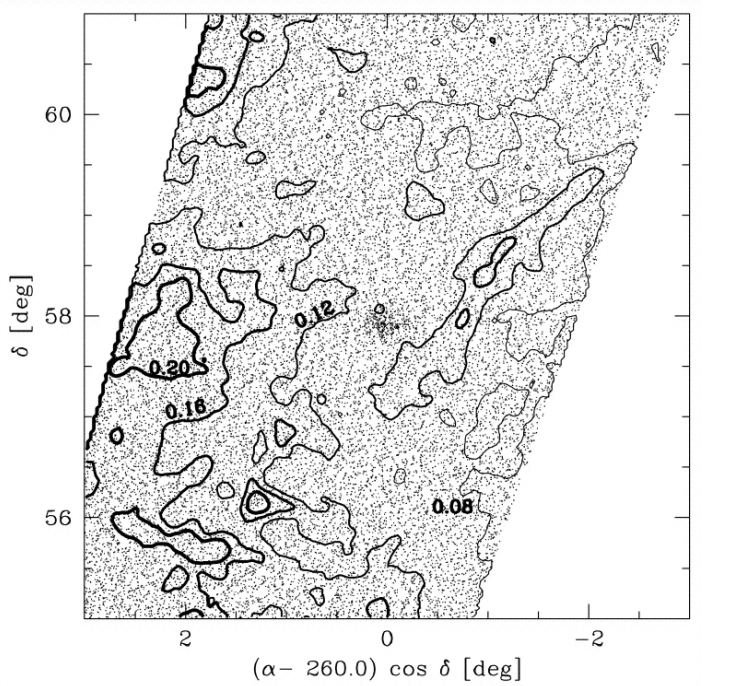

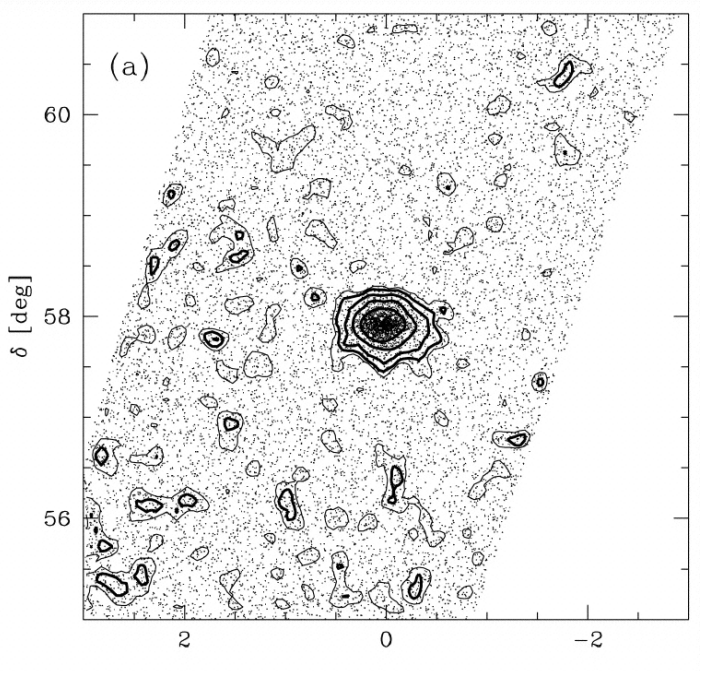

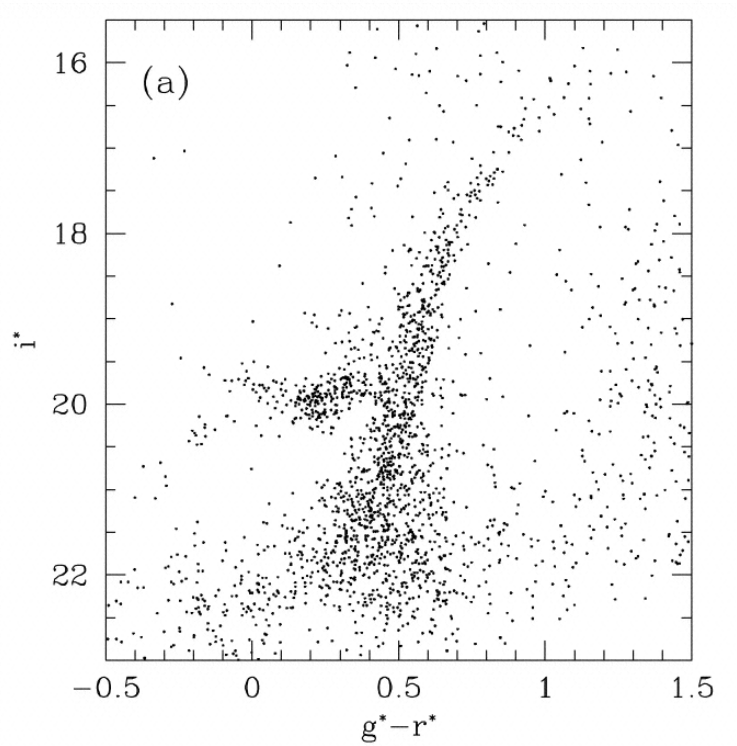

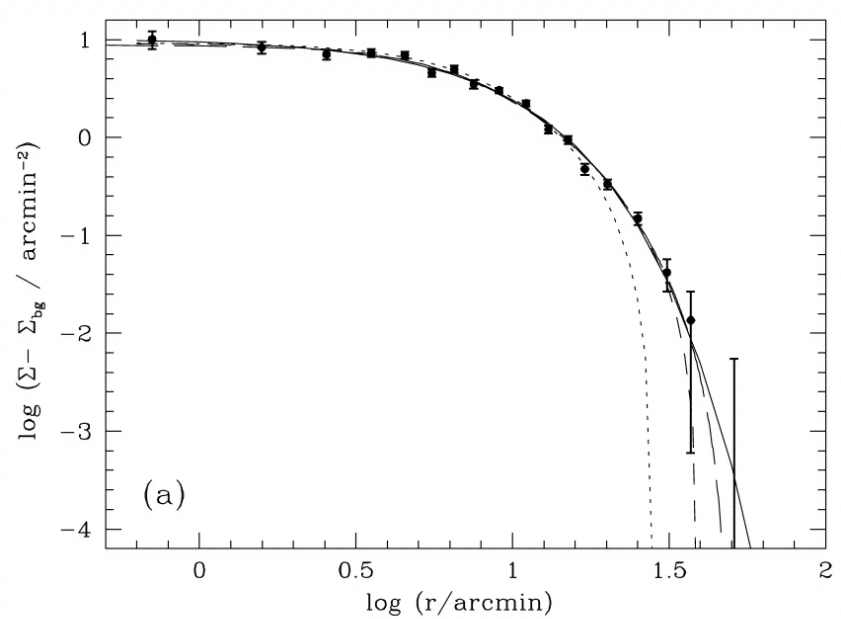

Odenkirchen et al. (2001)

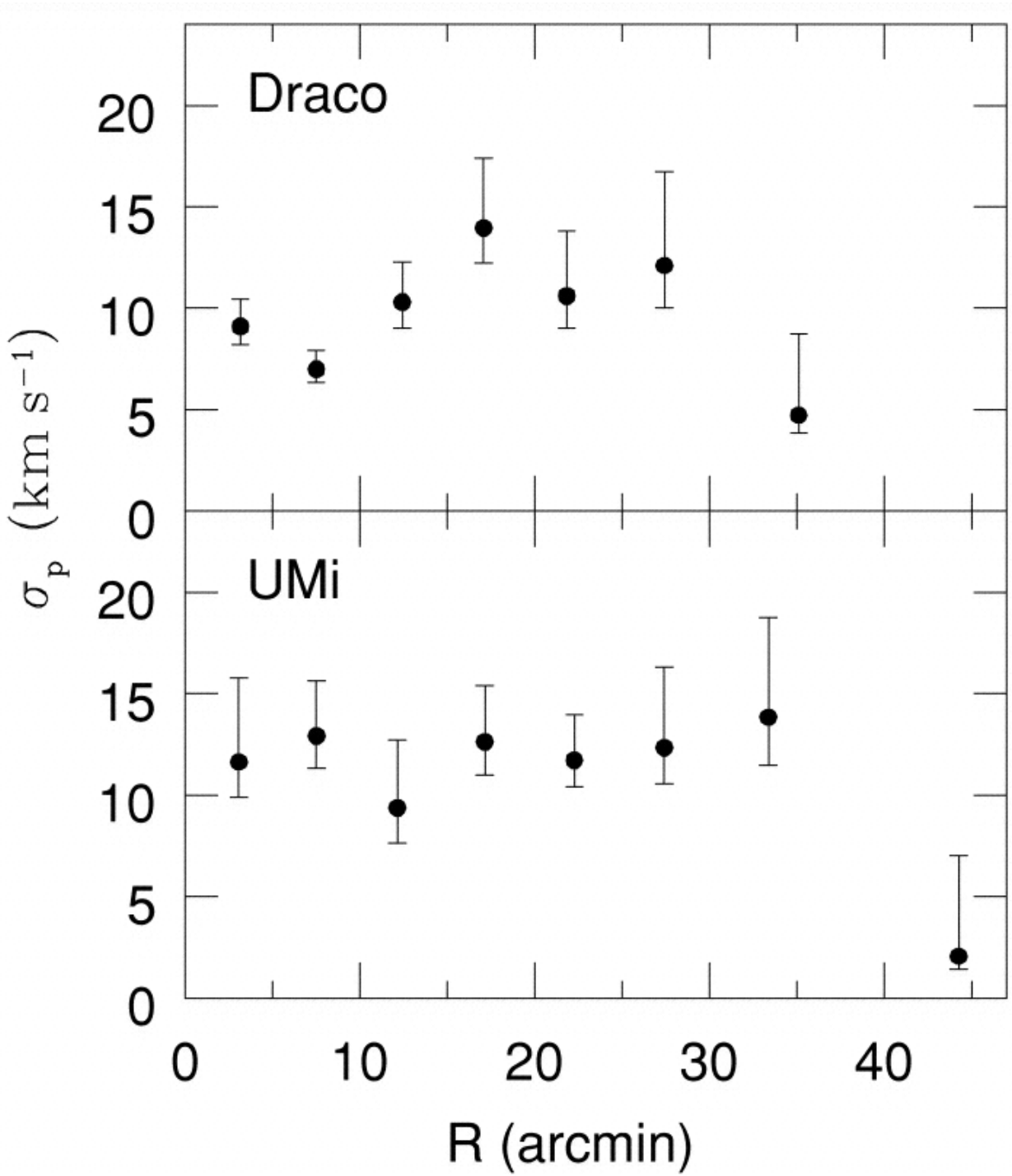

Wilkinson et al. (2004)

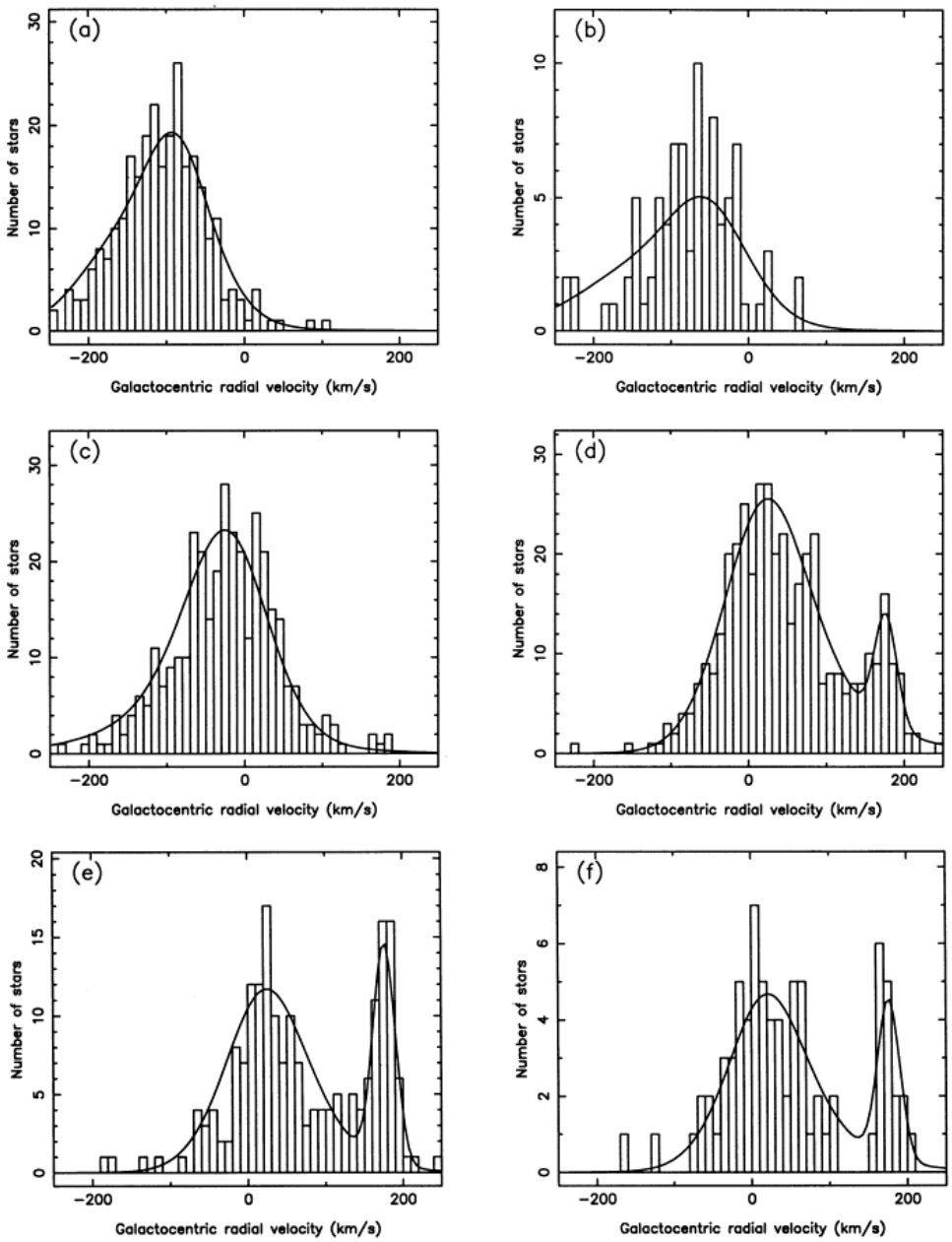

Figure 3. Comparison between the observed velocity distribution and that expected from the standard Galaxy model plus a Gaussian component of variable mean, dispersion and normalization which is included so as to account for the feature near 172 km s^{-1}. The lines of sight are the same as in Fig. 1.

©1995 RAS, MNRAS **277**, 781–800

Ibata & Gilmore (1995)

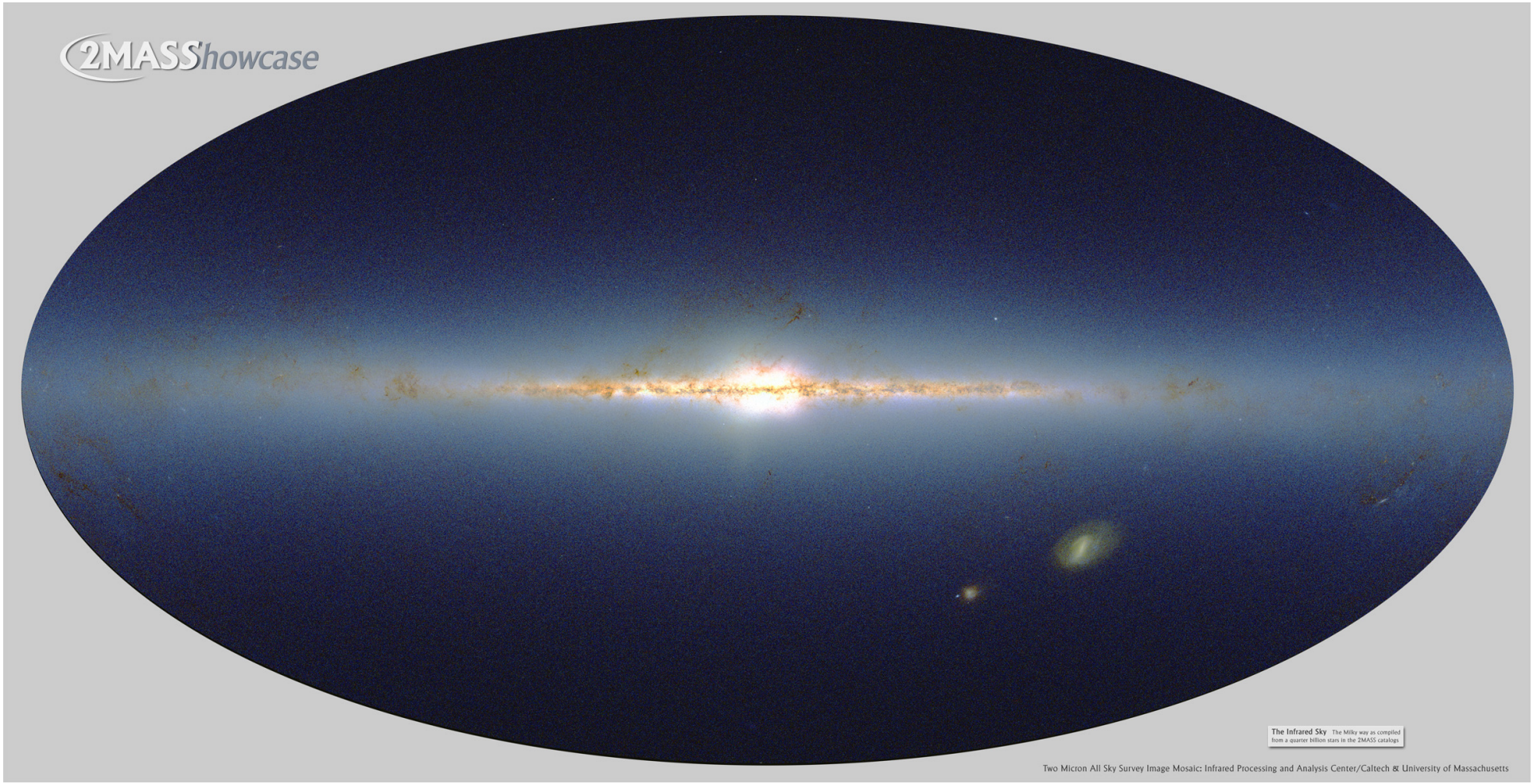
2MASSShowcase
The Infrared Sky The Milky way as compiled from a quarter billion stars in the 2MASS catalogs
Two Micron All Sky Survey Image Mosaic: Infrared Processing and Analysis Center/Caltech & University of Massachusetts

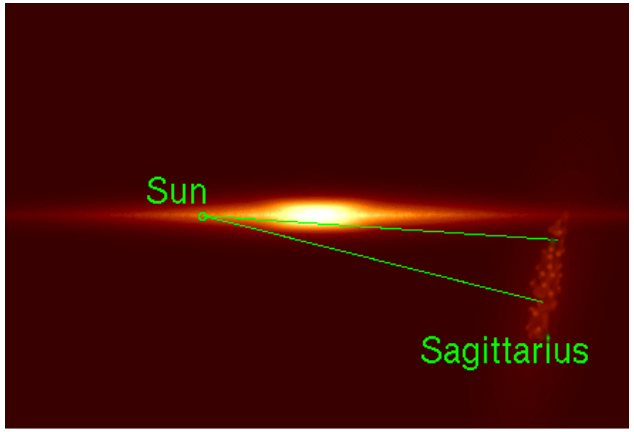
Sun
Sagittarius

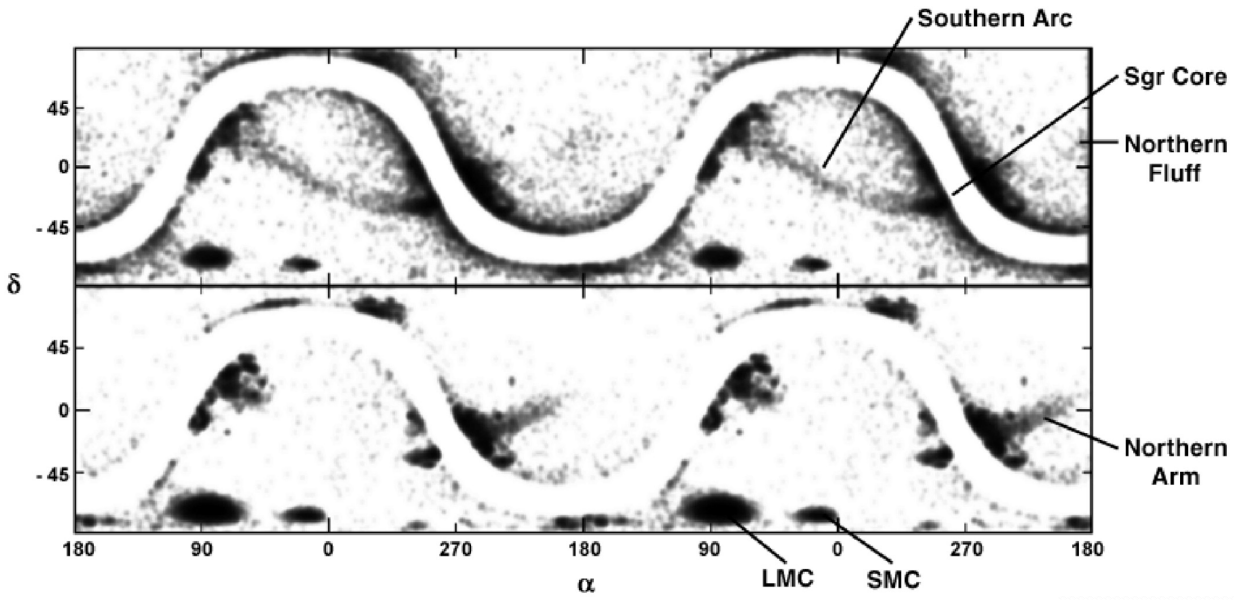

Majewski et al. (2003)

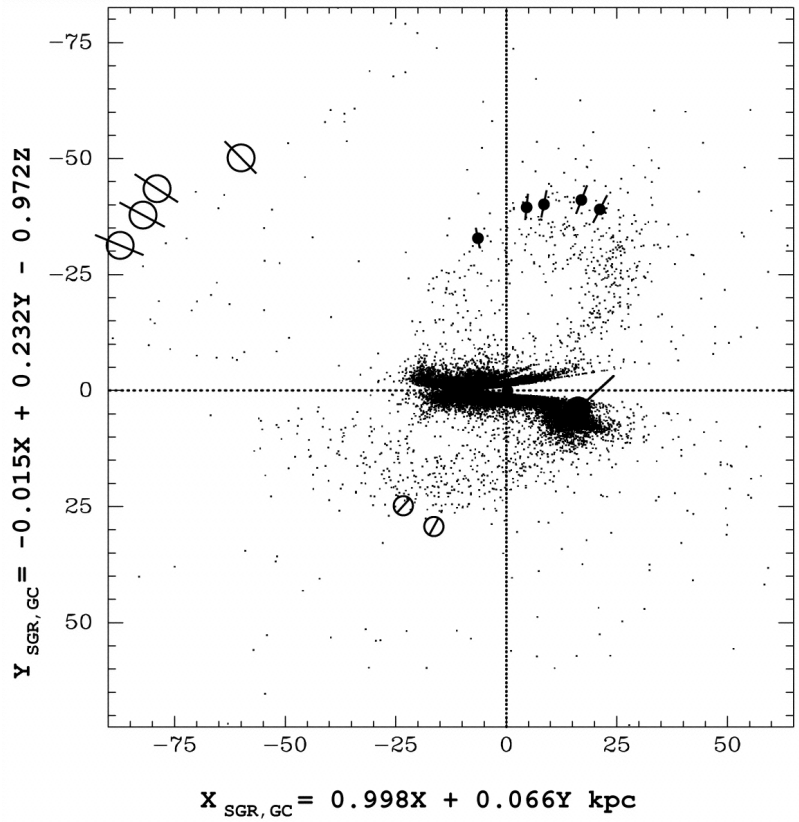

Newberg et al. (2003)

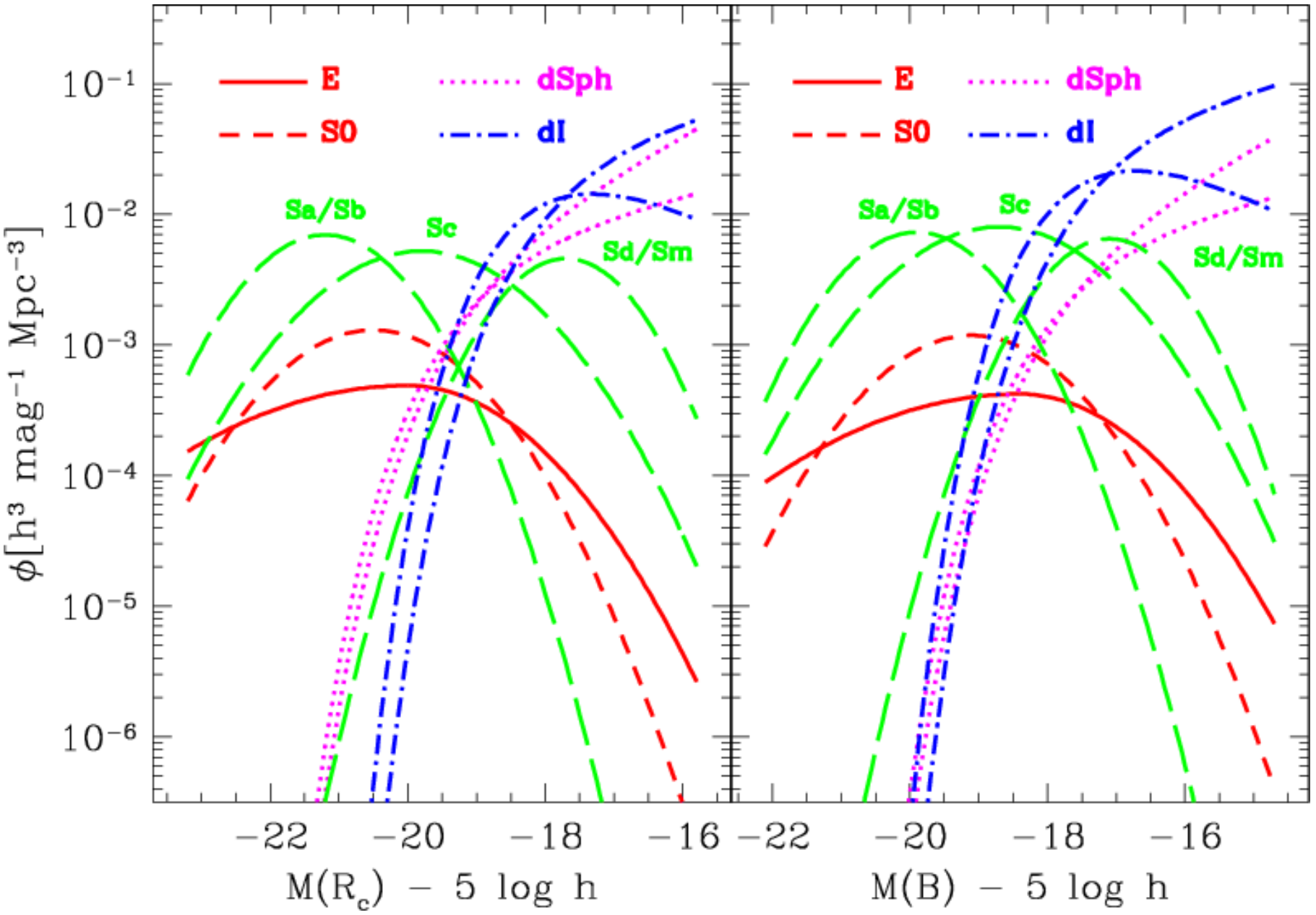

de Lapparent (2003)

Figure 5.1: PSF Surface Brightness. The percentage of the total flux at 4000Å falling on a PC pixel as a function of the distance from the peak of a star image.

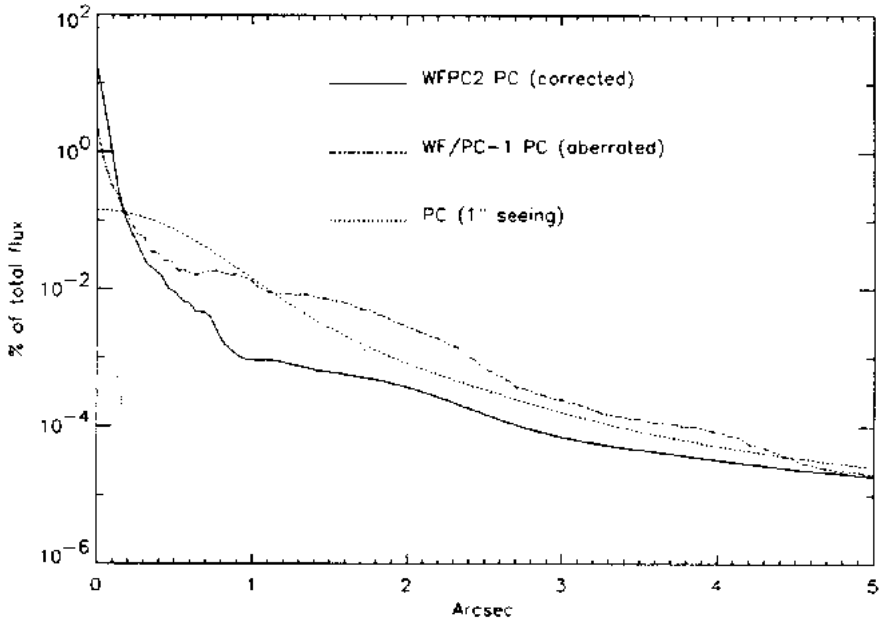

Figure 5.2: Encircled Energy. The percentage of the total flux at 4000Å within a given radius of the image peak.

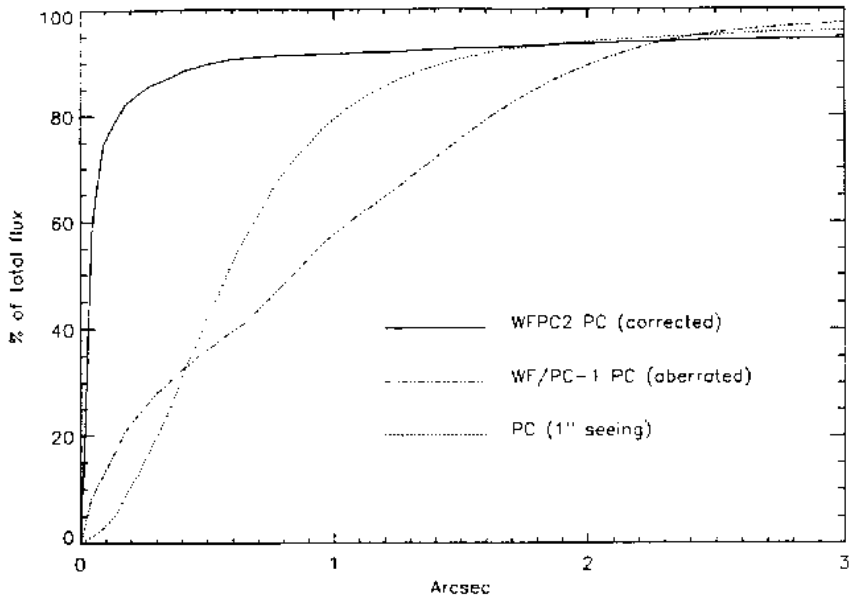

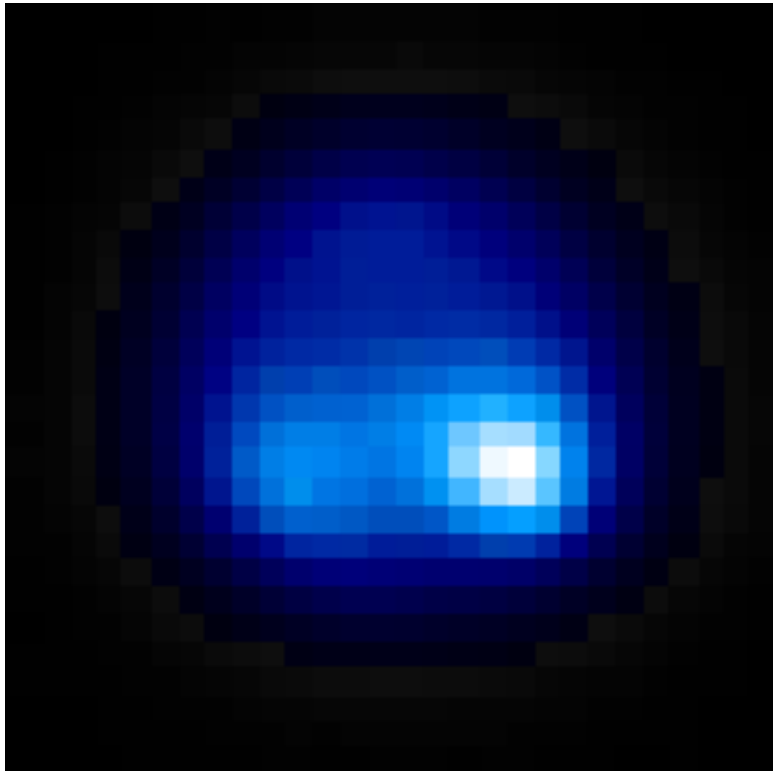

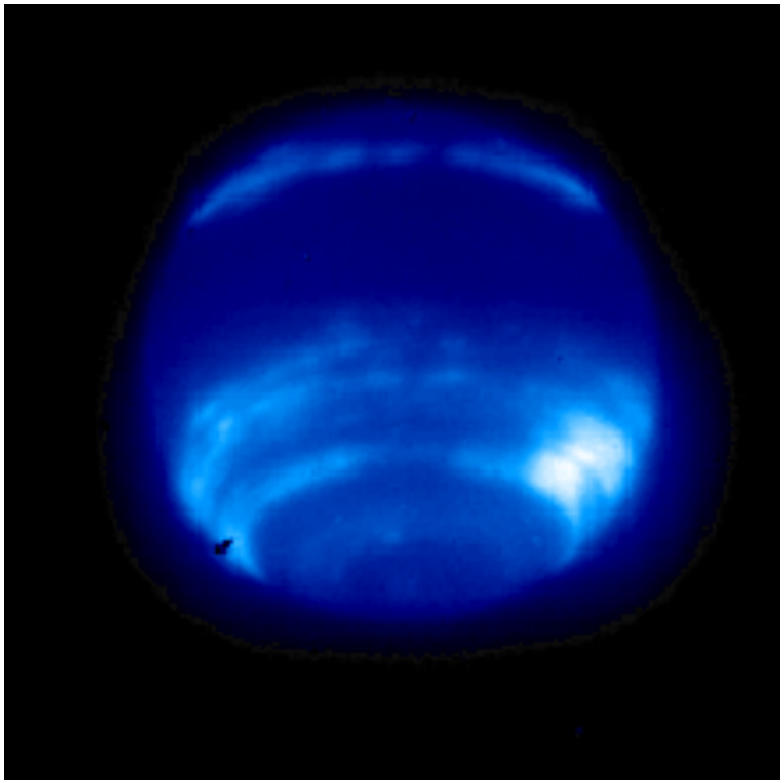

Neptune from the Keck Telescope, without and with AO at 1.65 microns

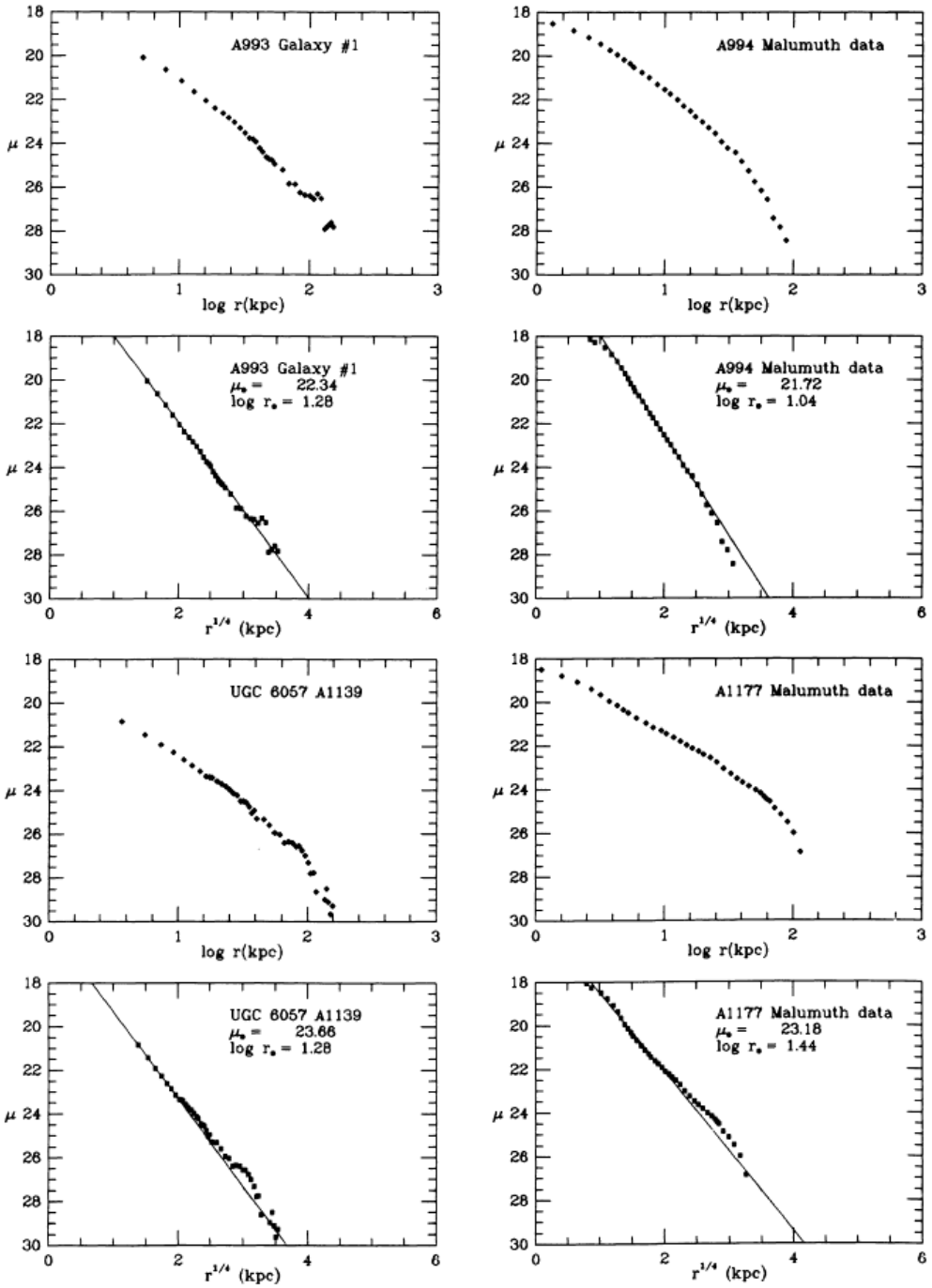

FIG. 1—*Continued*

Schombert (1986)

Dehnen (1993)

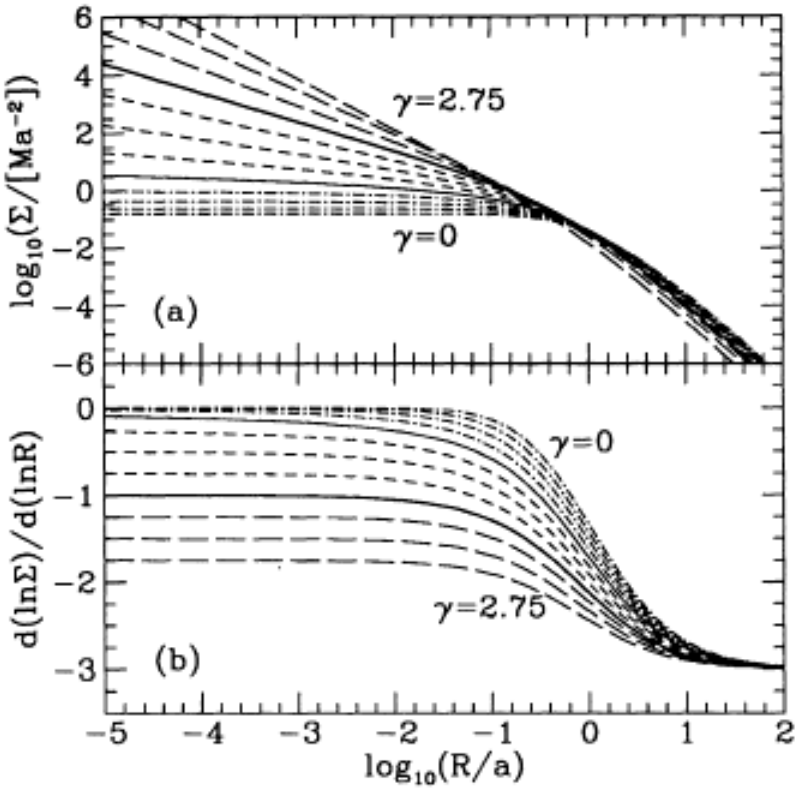

Figure 1. Surface density (a) and its logarithmic slope (b) for the mass models of equation (1). Dashed-dotted lines: $\gamma = 0$, 0.25,0.5,0.75; the thin solid line: Hernquist's model ($\gamma = 1$); dashed lines: $\gamma = 1.25,1.5,1.75$; the thick solid line: Jaffe's model ($\gamma = 2$); and long dashed lines: $\gamma = 2.25,2.5,2.75$.

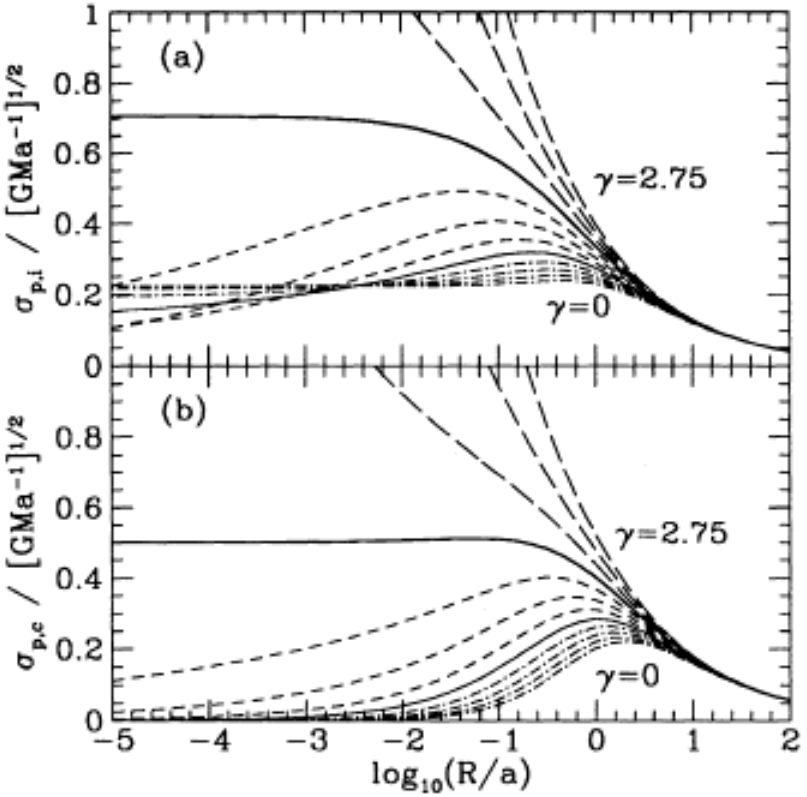

Figure 2. Profiles of the projected velocity dispersions of (a) isotropic and (b) circular models. The line styles are the same as in Fig. 1.

is $\sigma_{\rm p,i}^2 \propto R^{2-\gamma}$ for $\gamma \geq 3/2$ and $\sigma_{\rm p,i}^2 \propto R^{\gamma-1}$ for $1 \leq \gamma < 3/2$,

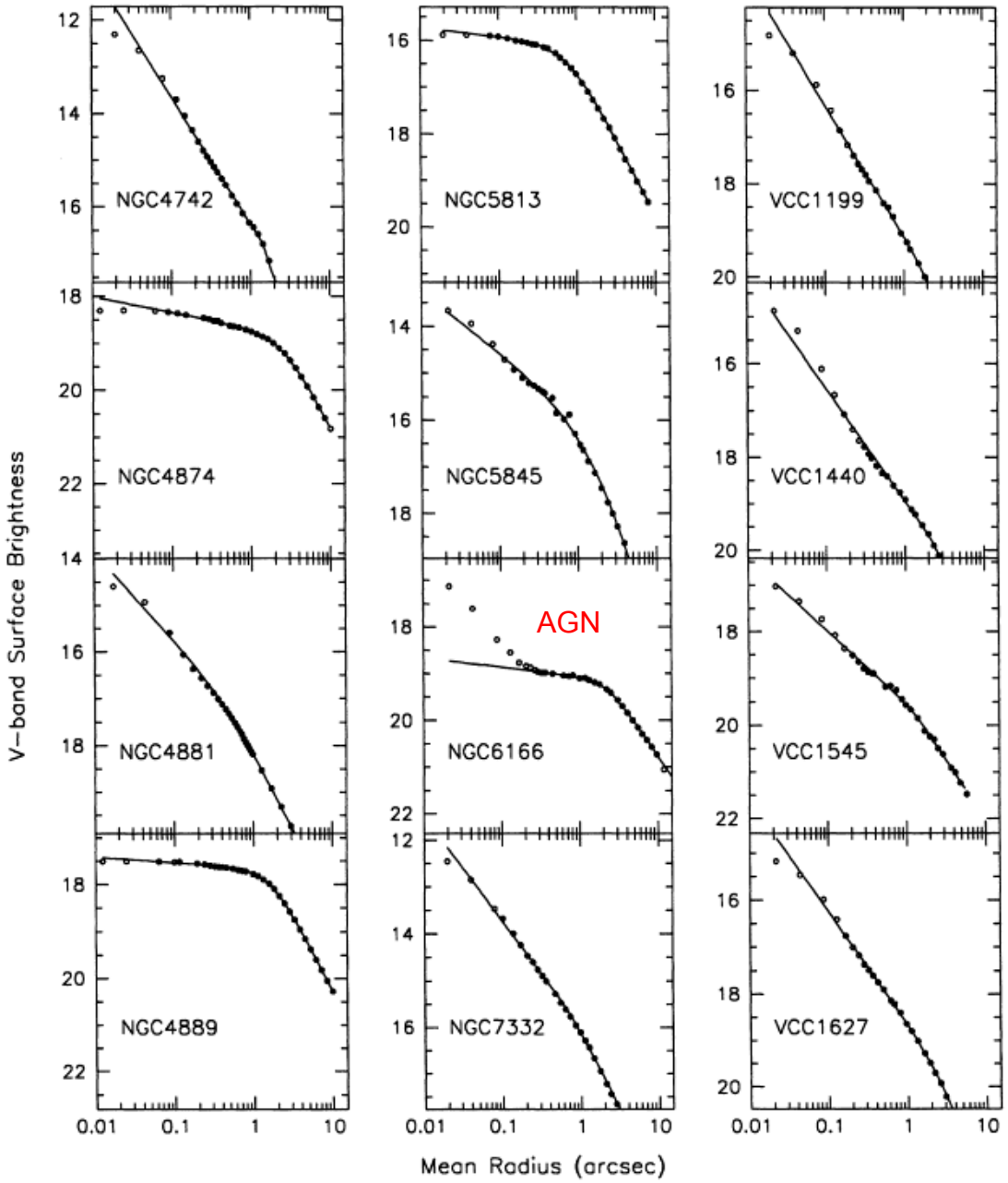

Nuker law

Byun et al. (1996)

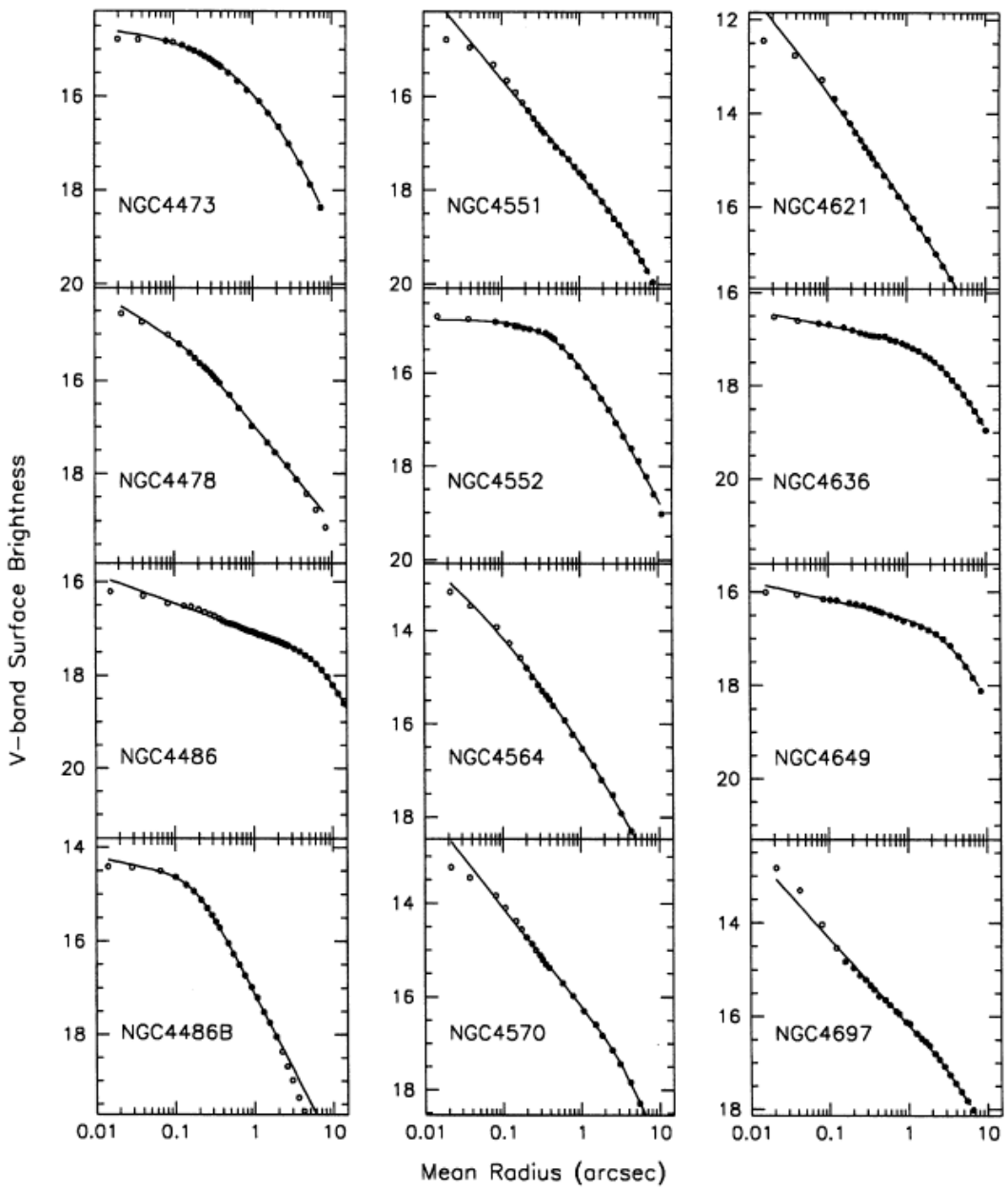

FIG. 3. (continued)

Nuker law

Byun et al. (1996)

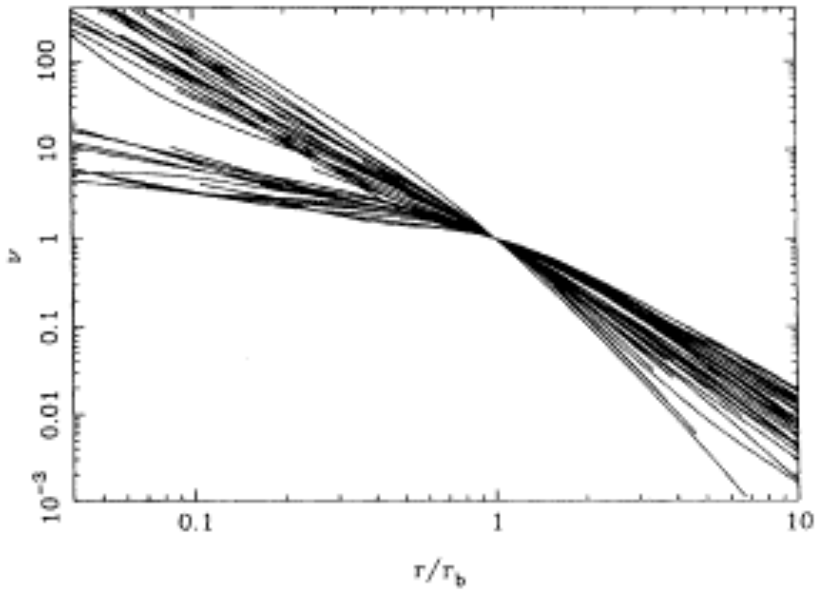

FIG. 3. Luminosity density profiles of all galaxies in the sample scaled to the radius and the luminosity at the radius of maximum curvature in the surface brightness.

Non-parametric fits to the luminosity density in elliptical galaxies

(Gebhardt et al. 1996)

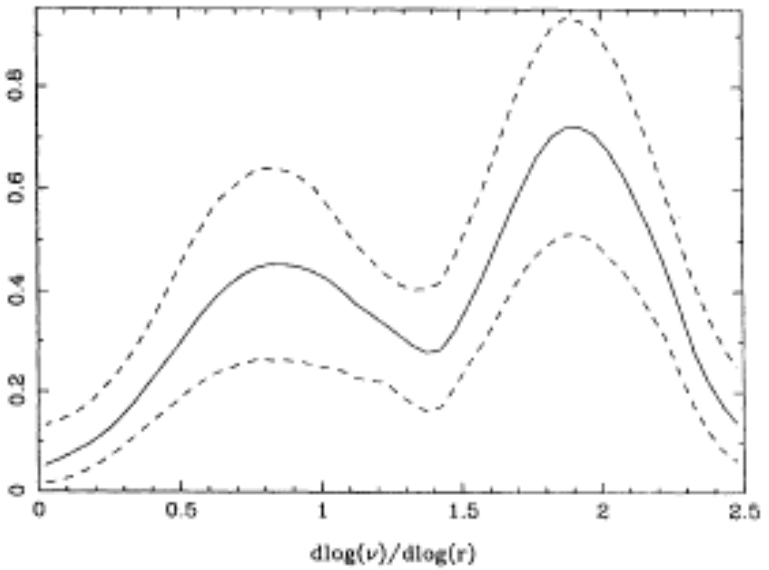

FIG. 2. Distribution function (solid line) for the logarithmic slope of the luminosity density, measured at $0.1^{\prime\prime}$. The dashed lines represent the 90% confidence band.

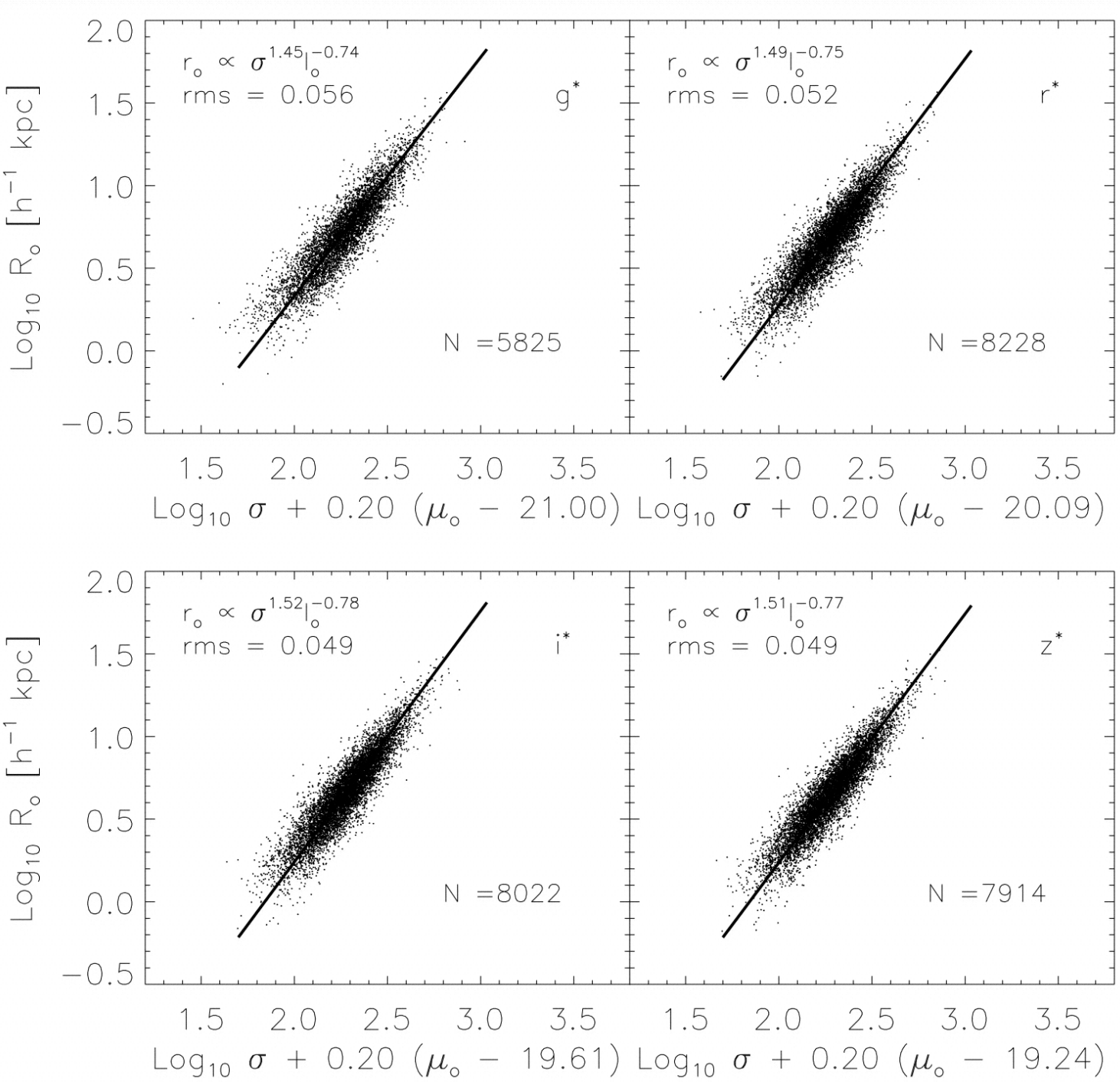

Fundamental plane from Bernardi et al. (2003)

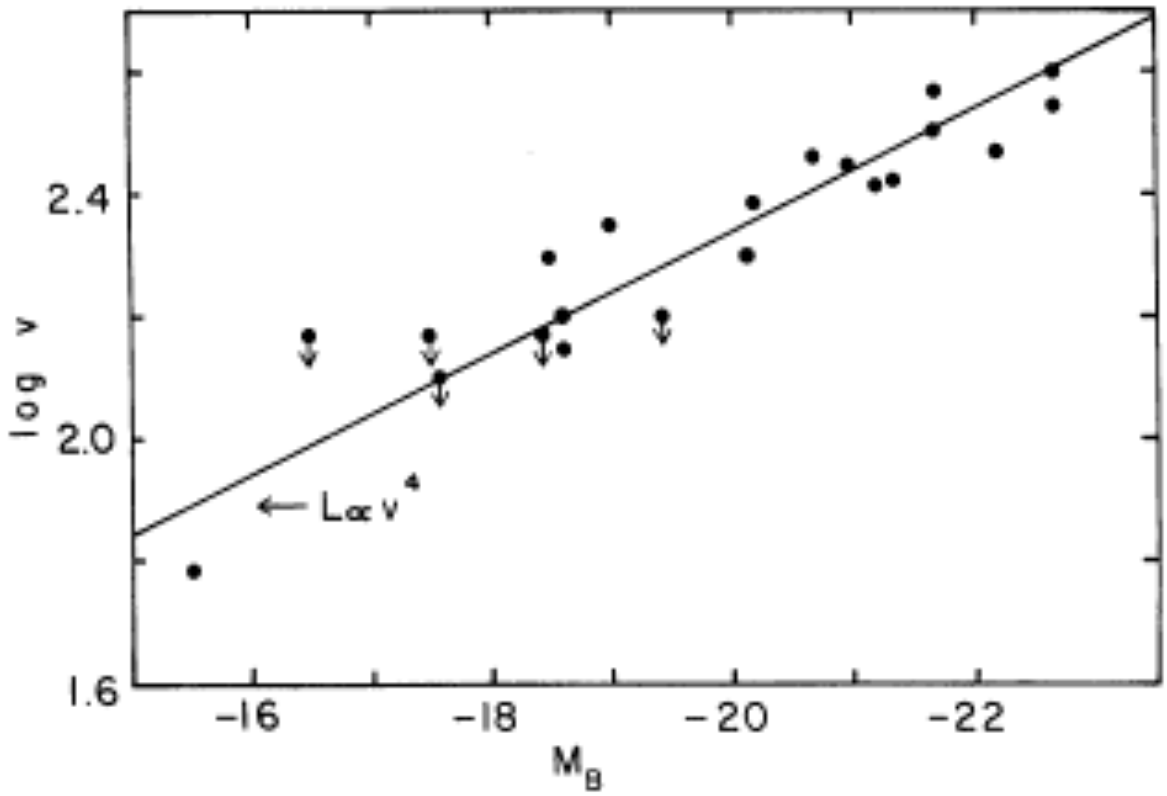

FIG. 16.—Line-of-sight velocity dispersions versus absolute magnitude from Table 1. The point with smallest velocity corresponds to M32, for which the velocity dispersion (60 km s^{-1}) was taken from Richstone and Sargent (1972).

Faber & Jackson (1976)

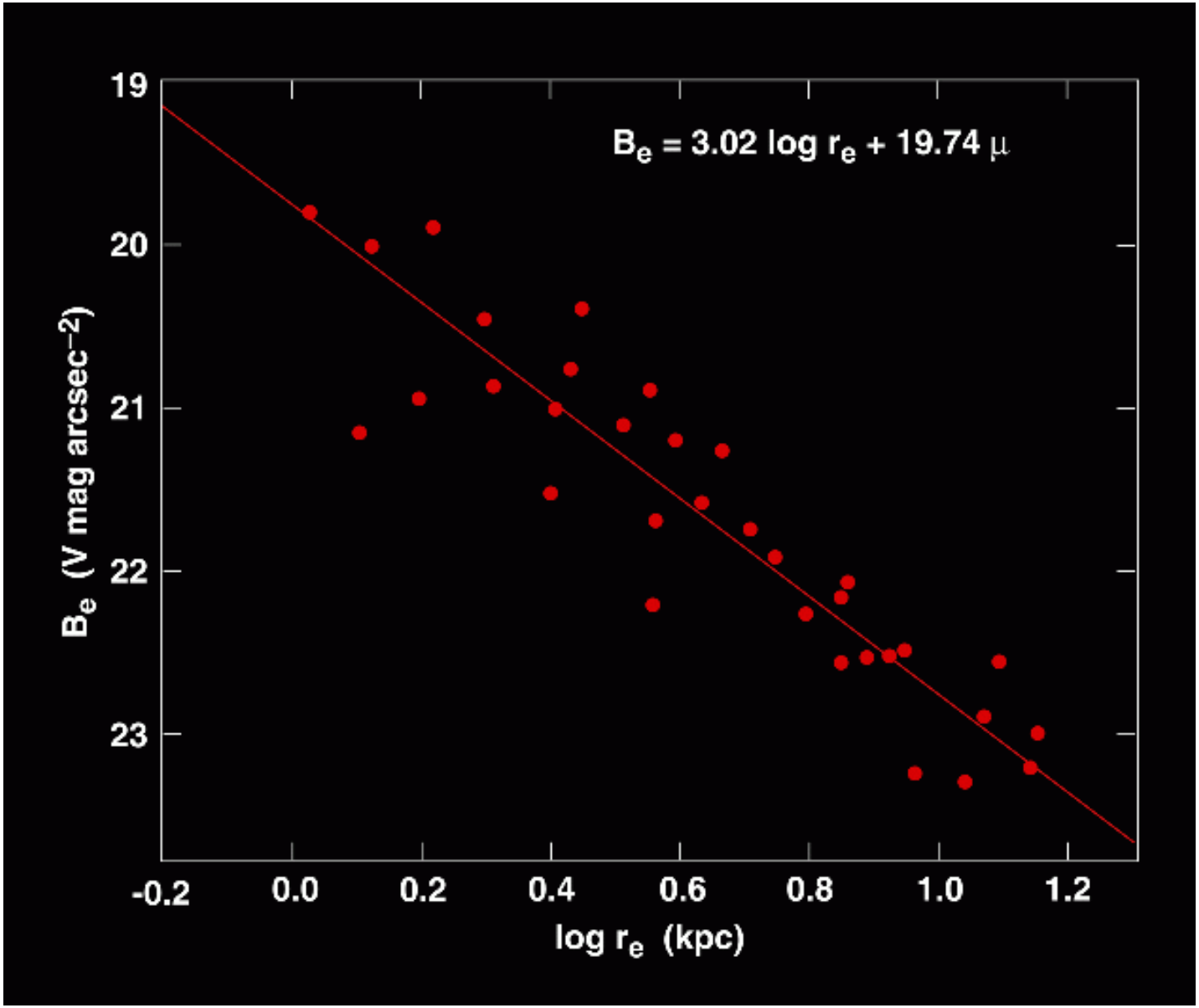

Kormendy (1977)

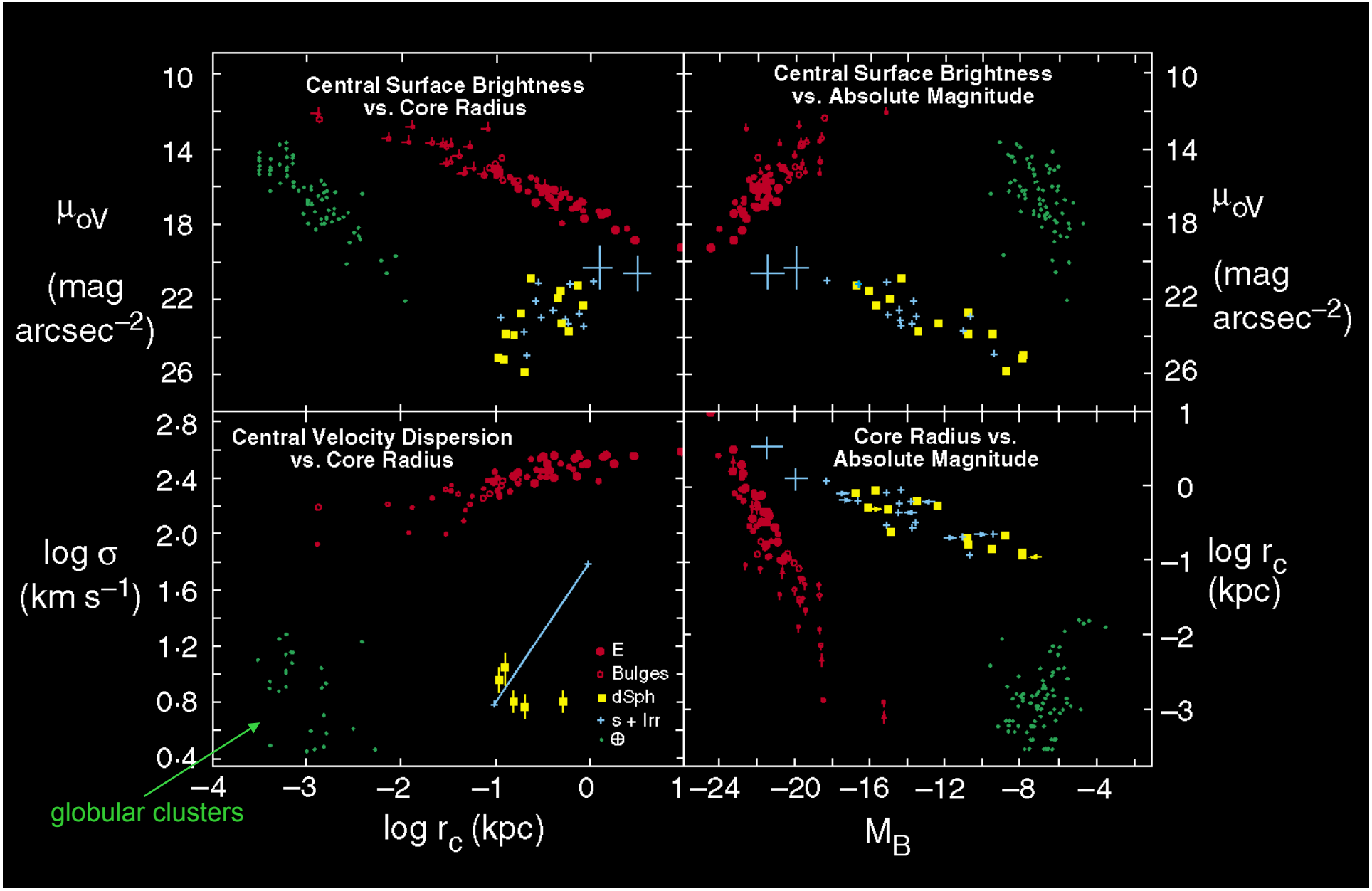

Kormendy (1987)